3D patient-specific spinal cord computational model for SCS management: potential clinical applications

Carmen Solanes[1,5]‡**, José L. Durá**[1]‡**, M Ángeles Canós**[2]**,**
Jose De Andrés[3]**, Luis Martí-Bonmatí**[4]**, and Javier Saiz**[1,5]

[1]Center of Research and Innovation in Bioengineering (Ci2B), Universitat Politècnica de València, Valencia, Spain
[2]Pain Unit, Hospital Universitari i Politècnic La Fe, Valencia, Spain
[3]Anesthesia, Critical Care, and Multidisciplinary Pain Management Department, General University Hospital, Valencia, Spain; and Anesthesia Unit- Surgical Specialties Department, Valencia University Medical School, Valencia, Spain
[4]Radiology Department, Clinical Imaging Area, Hospital Universitari i Politècnic La Fe, Valencia, Spain
[5]Corresponding author

E-mail: `carsogal@etsii.upv.es, jsaiz@ci2b.upv.es`

Abstract. *Background and objective:* Although Spinal Cord Stimulation (SCS) is an established therapy for treating neuropathic chronic pain, in tonic stimulation, postural changes, electrode migration or badly-positioned electrodes can produce annoying stimulation (intercostal neuralgia) in about 35% of the patients. SCS models are used to study the effect of electrical stimulation to better manage the stimulation parameters and electrode position. The goal of this work was to develop a realistic 3D patient-specific spinal cord model from a real patient and develop a future clinical application that would help physicians to optimize paresthesia coverage in SCS therapy.

Methods: We developed two 3D patient-specific models from a high-resolution MRI of two patients undergoing SCS treatment. The model consisted of a finite element model of the spinal cord and a sensory myelinated nerve fiber model. The same simulations were performed with a generalized spinal cord model and we compared the results with the clinical data to evaluate the advantages of a patient-specific model. To identify the geometrical parameters that most influence the stimulation predictions, a sensitivity analysis was conducted. We used the patient-specific model to perform a clinical application involving the pre-implantation selection of electrode polarity and study the effect of electrode offset.

Results: The patient-specific model correlated better with clinical data than the generalized model. Electrode-dura mater distance, dorsal CSF thickness, and CSF diameter are the geometrical parameters that caused significant changes in the stimulation predictions. Electrode polarity could be planned and optimized to stimulate the patient's painful dermatomes. The addition of offset in parallel electrodes would not have been beneficial for one of the patients of this study because they reduce

neural activation displacement.

Conclusions: This is the first study to relate the activation area model prediction in dorsal columns with the clinical effect on paresthesia coverage. The outcomes show that 3D patient-specific models would help physicians to choose the best stimulation parameters to optimize neural activation and SCS therapy in tonic stimulation.

Keywords: 3D patient-specific model, Spinal Cord Stimulation therapy, paresthesia coverage, clinical applications, computational model

1. Introduction

Spinal Cord Stimulation (SCS) therapy is a reversible and minimally invasive pain treatment aimed at reducing the intensity, duration and frequency with which pain is felt [1]. SCS has been clinically proven to be effective for treating a variety of chronic pain conditions that are refractory to current pharmacotherapies [2]. However, 35% of patients experience the common SCS side effect of intercostal neuralgia [3], caused by postural changes, electrode migration or badly-positioned electrodes, which can be resolved by readjusting the stimulation parameters [3, 4].

The basis of SCS therapy for tonic stimulation is well-accepted by the gate-control pain theory proposed by Melzack and Wall [5, 6, 7, 8]. According to this theory, the activation of large diameter, myelinated afferents (Aβ fibers) modulates the activity of small, unmyelinated afferents (C fibers) to modulate pain transmission information [9].

Based on this theory, computational spinal cord modeling has become a useful tool to study the effect of electrical stimulation on neural response [10, 11, 12, 13]. More detailed computational spinal cord models were developed as the technology advanced. For example, in 2014, two spinal cord models were created as extrusions of average adult human lower thoracic measurements obtained from preoperative patients' MRI [14, 15]. In 2018 our research group developed a T10 vertebral level spinal cord model [16]. The novelty of this generalized model was that it included the spinal cord offset in the spinal canal and the geometrical parameters were taken from *in vivo* high-resolution human spinal cord measurements [17]. Khadka et al. later developed an open-source spinal cord model with detailed information for every tissue compartment [18], and Viljoen et al. developed a model which includes relevant structural dimensions from T4 to T10 vertebral levels and the dorsal root entry zone dorsal arc length [19]. Lempka *et al.* have recently proposed the first patient-specific spinal cord model which predicts sensory thresholds consistent with the clinical measurements. However, the spinal cord dimensions of the model are the average patient measurements of the T9 spinal cord anatomy [20]. As the electrodes can be located at different vertebral levels, using average measurements for the geometrical parameters in the computational models and

including only one vertebral level may limit the results obtained, since it is not possible to reproduce the location of the electrodes within the spinal cords of individual patients.

SCS computational modeling is currently evolving into patient-specific modeling. In the spinal cord geometry at each spinal level, the size and shape of the spinal cord and spinal canal, the relative location of the spinal cord within the spinal canal and the amount of CSF between the epidural location of the SCS lead and the dorsal column (DC) fibers all vary between patients. All these geometrical parameters play a significant role in selecting the programming parameters (polarity, amplitude, pulse width and frequency) to optimize neural activation, i.e. paresthesia coverage, for individual SCS patients [21].

In this context, the aim of this study was to develop a more detailed 3D patient-specific spinal cord model which included the authentic anatomical structure and spinal cord dimensions of the different vertebral levels at which percutaneous electrodes are usually implanted (from T8 to T10). We also used our previously developed generalized model [16] to compare the approximation of both models to two real cases. We performed a sensitivity analysis to identify the spinal cord geometrical parameters that most affect the stimulation predictions. The paper includes a case study of the proposed application of the patient-specific SCS management model.

2. Methods

2.1. Volume conductor models

2.1.1. Generalized spinal cord model The generalized model [16] consists of the following tissues: white and grey matter, cerebrospinal fluid (CSF), dura mater, epidural

Table 1: **Electrical conductivities of the tissues considered in the volume conductor models.**

Tissue	Electrical conductivity (S/m)	References
Grey matter	0.23	[22, 23, 24]
White matter, transversal	0.083	[22, 23, 24]
White matter, longitudinal	0.6	[22, 23, 24]
Cerebrospinal fluid (CSF)	1.7	[22, 23, 24]
Dura mater	0.03	[8, 25]
Fat	0.04	[22, 23, 24]
Bone	0.02	[23, 8]
Poles (platinum-iridium alloy)	$5.273 \cdot 10^6$	[26]
Insulator	0.002	[8]
Electrode-tissue interface	0.15	[27]

fat and bone (see figures 1a and 1b). The electrical conductivity of the different tissues are shown in Table 1. The geometry of the published model refers to T10 vertebral level, but as the stimulation was tested to the real patients at the three vertebral levels (T8, T9, and T10) the geometrical model parameters were also adapted to T8 and T9 using the mean values of *in vivo* human spinal cord measurements [17]. Further details of the geometrical parameters can be seen in figure S1 and Table S1 in Supplementary information (Section 1).

The electrodes were modeled as eight-pole percutaneous leads located in the epidural space (see figures 1d and 1f). The electrode-tissue interface was included as a 0.1-mm thick hollow cylinder with 0.15 S/m electrical conductivity [16] covering the active electrode poles. The model's electrode bipolar impedance was approximately 1 kΩ, consistent with clinical bipolar impedance measurements, so that a conversion of 1 V to 1 mA can be used as an approximation of the relative current-controlled stimulus magnitudes for the voltage-controlled stimulation. In order to simulate the neural activation of the patient using the generalized volume conductor model, electrodes were in the same position as implanted in the real patient, using the X-ray of the electrodes taken during the implantation procedure as a reference (see figures 1c and 1e).

2.1.2. Patient-specific spinal cord model Preoperative 3T high-resolution MRI scans were used without contrast media administration of the thoracic spine to obtain the patient-specific spinal cord anatomy. The scans consisted of T2-weighted and T1-weighted images with a sagittal orientation, as seen in figures 2a and 2b, where white matter, CSF, fat tissue (epidural space) and vertebral bone can be differentiated. The sagittal T2-weighted and T1-weighted images were obtained using the protocol for spinal cord MRI acquisition from the Standard Operating Procedure (SOP) given by De Leener *et al.* [28] (T2-weighted image parameters: scanning sequence = cube, magnetic field = 3T, field of view = 25.6 mm, number of slices = 60, slice thickness = 0.8 mm. T1-weighted image parameters: sequence = SPGR, magnetic field = 3T, field of view = 32 mm, number of slices = 60, slice thickness = 1 mm). The scans were obtained with the patient in supine position. The *Spinal Cord Toolbox (SCT)* developed by De Leener *et al.* [28] was used to automatically segment the CSF layer and white matter from T8 to T10. Figures 2d and 2e show the superimposed white matter and CSF segmentations with the T2w MRI. Both segmentations were verified by visual inspection. MR images were obtained at the *Hospital Politècnic i Universitari La Fe* using General Electric equipment.

Bone segmentation was performed manually on Seg3D software in 40 0.8 mm thick cuts of the MR image to segment the vertebral bones.

All the segmentations (bone, CSF and white matter) were smoothed by Amira software to reduce meshing and geometrical errors for solving the FEM model in COMSOL Multiphysics. Figure 2c shows the raw segmentation of the vertebral bone obtained from

(a) Axial view.

(b) 3D view.

(c)   Radiography. Antero-posterior (AP) view.

(d)   AP view.

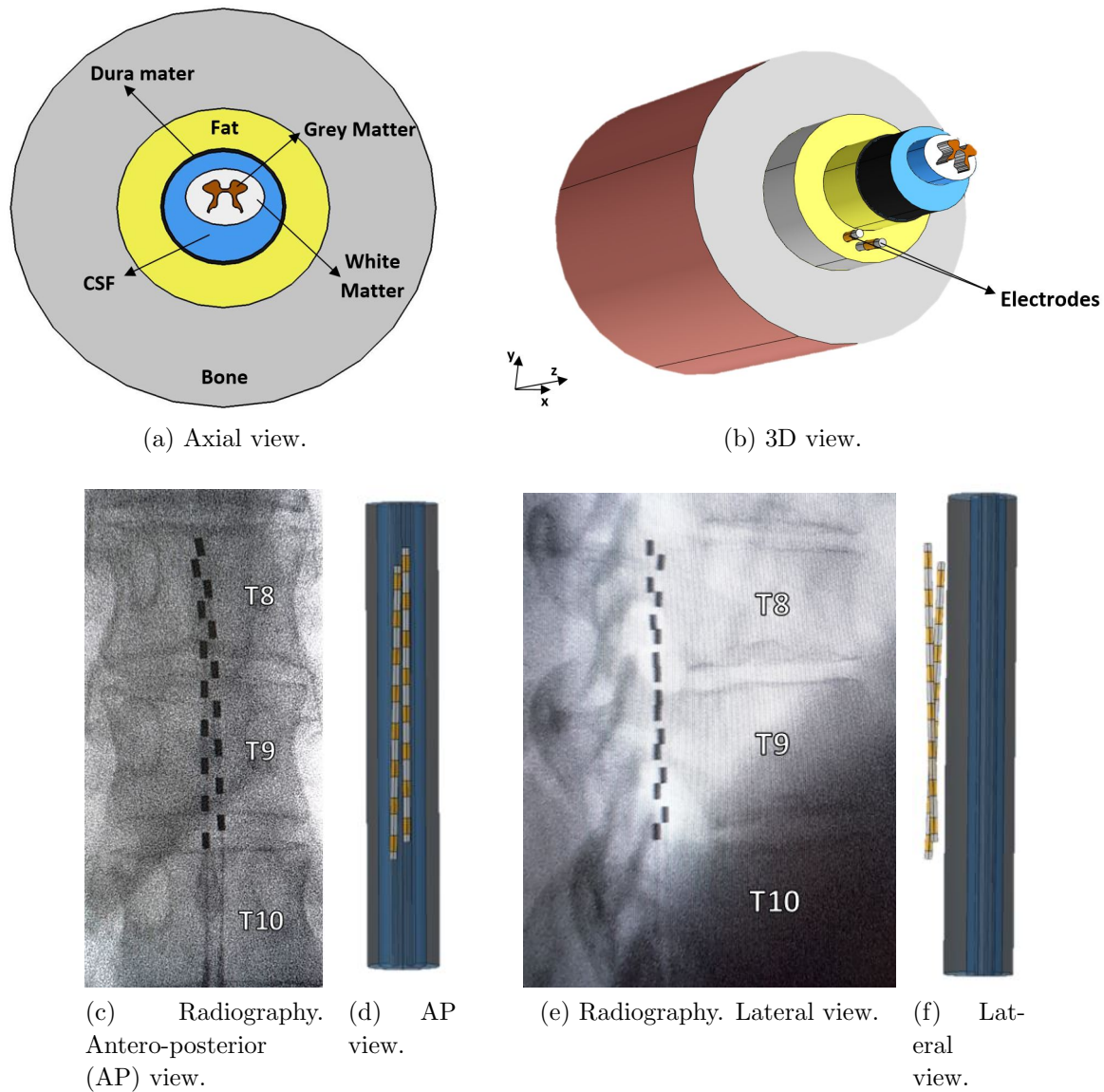(e) Radiography. Lateral view.

(f)   Lateral view.

Figure 1: **The generalized spinal cord model and electrode X-ray.** Fat and bone tissues are hidden to show the location of the electrodes in the computational model. The model's spinal cord geometry is that of T9 (a) and b)). Percutaneous electrode dimensions: length: 53 mm; diameter: 1.3 mm; pole length: 3 mm; intercontact length (insulator): 4 mm; number of poles: 8. X-ray of the electrode taken from the patient (c) and e)), and the location of the electrodes in the generalized spinal cord model (d) and f)).

Seg3D software and figure 2f shows the result of the smoothing process, with notably reduced sharp edges.

The segmentations were imported to COMSOL Multiphysics software to calculate the electric field distribution in the spinal cord. Dura mater was not segmented from the patient's MRI since the image resolution was not good enough to differentiate it from

(a) T2w image. Sagittal view.

(b) Axial view

(c) Vertebraes segmentation.

(d) White matter (red) and CSF (blue) segmentations. Sagittal view.

(e) White matter (red) and CSF (blue). Axial view.

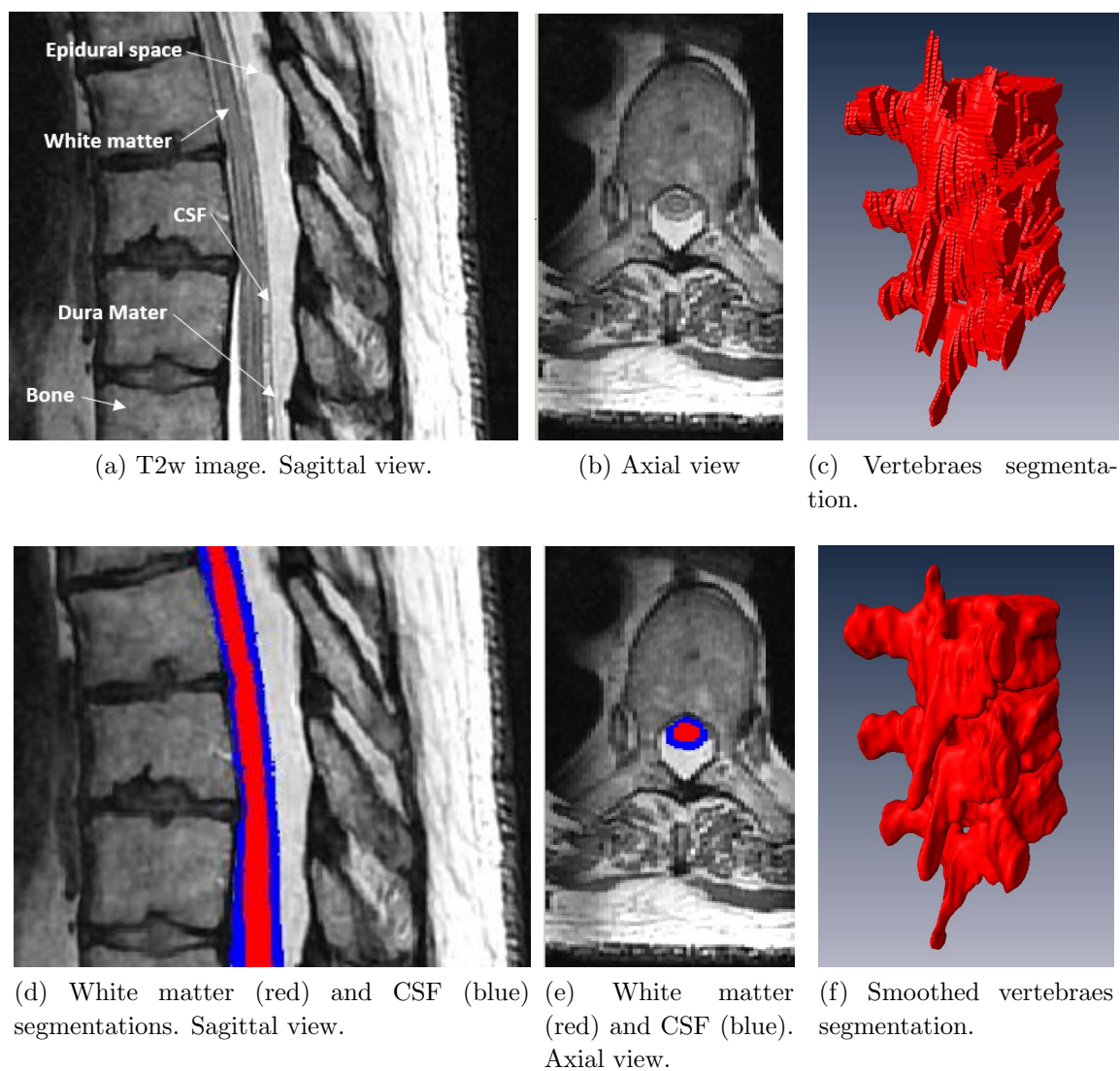(f) Smoothed vertebraes segmentation.

Figure 2: **White matter, CSF and vertebral bone segmentations.** CSF: cerebrospinal fluid. (c) and (f) are images taken from Amira software.

the rest of the tissues. However, based on previous studies [29, 30, 31], the maximum value of the dura mater thickness in the human spinal cord at the L2-L4 levels is 0.3 mm. Therefore, dura mater was included in the model by creating in COMSOL Multiphysics a layer of 0.3 mm thick that covers the CSF. Fatty tissue was included by adding a cylinder to cover the entire spinal canal. The dorsal root (DR) anatomy was not included explicitly, following Zander et al. [31], who stated that the anatomy of the dorsal rootlets can be ignored in FEM design. As we were interested in the activation of the DC nerve fibers, grey matter was not included in the volume conductor model to reduce the computational cost. In order to confirm that excluding the grey matter did not produce differences in the model predictions, we performed a sensitivity analysis, which suggested that the grey matter could be ignored in the FEM design, since there

(a) Axial view.

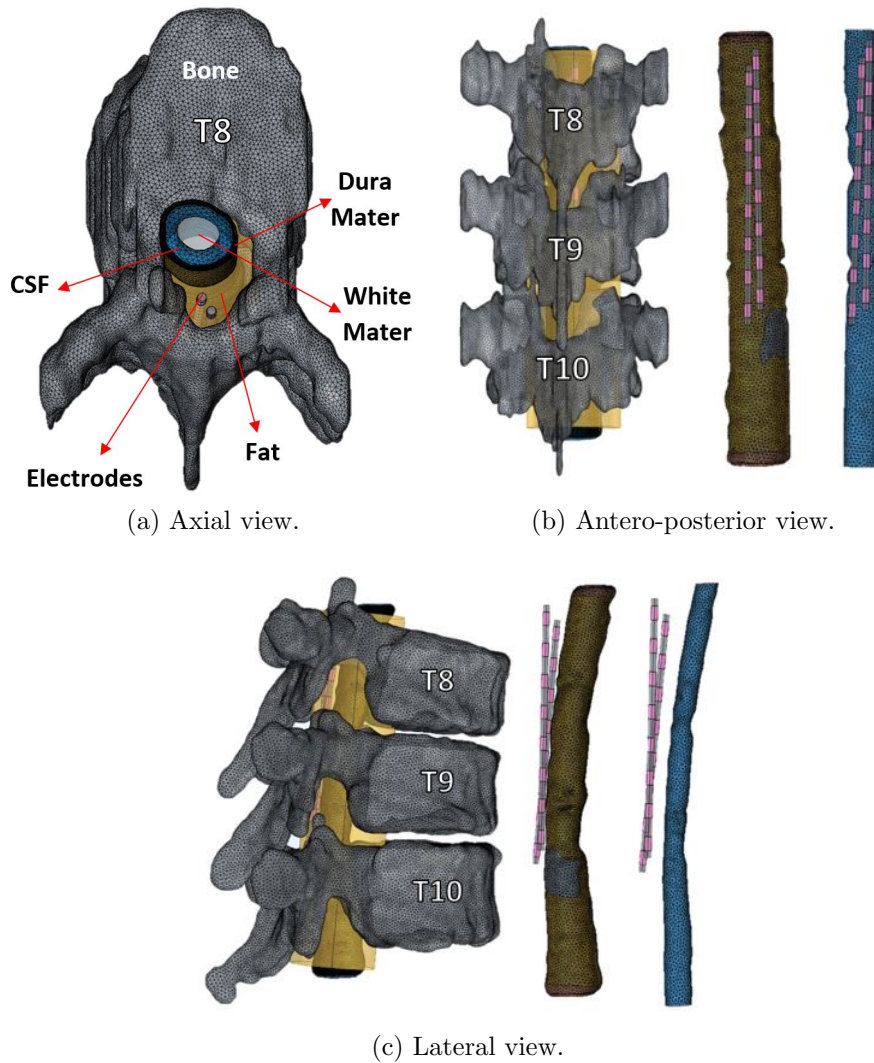(b) Antero-posterior view.

(c) Lateral view.

Figure 3: **Patient-specific spinal cord model.** In the central images of Figures (b) and (c), bone and fat tissues are hidden. In the left-hand images of Figures (b) and (c), dura mater and CSF are also hidden. CSF: cerebrospinal fluid. Percutaneous electrode dimensions: length: 53 mm; diameter: 1.3 mm; pole length: 3 mm; intercontact length (insulator): 4 mm; number of poles: 8.

were small errors in the perception thresholds for the DC (PT_{DC}) and DR (PT_{DR}) nerve fibers, and thus, the activating area (AA) (see Section 1 and Table S2 in Supplementary information). However, the grey matter segmentation was used to locate the DR nerve fibers (see Section 1 and figure S2 in Supplementary information for further details).

The electrodes were included in the epidural space (fat tissue) (see figure 3a, 3b and 3c) and were located using the patient's X-ray, as described in the generalized model. The patient-specific model assumes the same tissue electrical conductivities (shown in Table 1) as the generalized model. For further information on the geometrical parameter values of the two patient-specific models see Supplementary information (Section 1).

A tetrahedral adaptive mesh was used in both models to avoid errors in the narrow and edge zones. The generalized model used just under 3,800,000 elements with a maximum element edge length of 1.94 mm and a minimum of 0.05 mm. In the white matter tissue, the edge length ranged between 50-194 μm. The patient-specific model used around 12,300,000 elements, with a maximum element edge length of 2.4 mm and a minimum of 0.024 mm. The white matter element edge length ranged between 24-240 μm. According to Arle et al. [24] these mesh resolutions are accurate enough to resolve axons electrically down to the dimension of their internodal distances. For further details of the boundary conditions and mesh properties, see Section 4 (Table S3) in Supplementary information.

2.2. Myelinated nerve fiber model

According to the gate control theory of pain postulated by Melzack and Wall [9], DC sensory Aβ fibers are most likely to be affected by SCS. We therefore used a myelinated nerve fiber model in a combination of the two most widely used nerve fiber models in SCS studies: the Wesselink-Holsheimer-Boom (WHB) model [32] and the Richardson-McIntyre-Grill (RMG) model (model B) [33].

The membrane dynamics is based on the WHB model, which includes fast potassium channels, sodium channels and leakage channels. The membrane dynamics parameters were calibrated to replicate human sensory axons by the Holsheimer's group [32]. In this work we included the myelin as an imperfect insulator whose electrical parameters are based on the cable model from the RMG nerve fiber model B [33]. The RMG nerve fiber model B is physiologically accurate (it matches experimental data for both the excitation and the conduction properties), and it is suitable for studies where the effect of depolarising afterpotentials (DAPs) is not relevant [33]. The differential equations and the values of the electrical parameters are described in Supplementary information (Section 2, see Table S3).

The model parameters were calibrated to match the human experimental data of the action potential shape. Stimulating a 12-μm nerve fiber, the conduction velocity obtained is 46 m/s, a value within the physiologic range (12-70 m/s) [34, 35, 36]. The absolute refractory period is 0.67 ms and the relative refractory period 2.69 ms, within the experimental ranges measured in human median and sural nerves ((0.58-0.79 ms) and (2-3.95 ms), respectively) [37]. The simulation by the model of an action potential generated in a 12-μm nerve fiber node can be seen in Supplementary information (see Section 2, figure S3) in addition to an electric diagram of the model.

The fiber diameter of afferent Aβ fibers in human DC ranges between 1-15 μm [38, 39]. The large axon diameters (> 11.5 μm, i.e. from 12 to 15 μm) increase sig-

nificantly from the midline to DR entry zone [38, 40]. Thus, although 12.8-μm axon diameter has a low density in the DC [38], we can assume that the largest fibers recruited first in the DC have a diameter of 12 μm and 15 μm in the DR [7, 10, 11, 12, 22, 41], since the highest axon diameters are located in the dorsolateral columns and are farther from the stimulation electrode [38]. As experimental morphology measurements are available for 12.8 and 15-μm axon diameters [42], both the generalized and patient-specific spinal cord models included a population of 12.8-μm axon diameter in the DC and 15-μm axon diameter in the DR (see Supplementary information (Section 3).

2.3. Model output parameters

The simulation procedure was divided into four steps, as shown in figure 4. First, using COMSOL Multiphysics, we defined the electrode polarity by assigning as anode (positive electric voltage) or cathode (negative electric voltage) the poles we want to program. The electric field distribution was then calculated and the activating function represented on the surface of the spinal cord, since it gives information on the most likely position of neural activation (shown in red in figure 4 (Step 1)) [43, 44]. The second step consists of importing the electric potential values at each node of Ranvier and internodes so that the internodal distance of the nerve fiber considered in the DC nerve fiber distribution (12.8 μm) and in the DR (15 μm) determines the selection of the points of the electric potential value and position of the node of Ranvier (in x, y and z-axis). As shown in figure 4 (Step 2), in the axial view of the nerve fiber distribution, each point is a transversal projection of a nerve fiber whose location depends on the spinal geometry (see figures S4, S5 and S6 in Supplementary information). When solving the differential equations of the nerve fiber model, we can obtain an action potential propagation (the nerve fiber is activated) or a subthreshold response (the nerve fiber does not fire an action potential), so we assign red to activated and blue to not activated nerve fibers (see figure 4 (Step 3)). For DR nerve fibers, as well as for DC fibers, the corresponding FEM solutions are coupled to multicompartment cable model of sensory dorsal roots. Therefore, Step 1 and Step 2 are followed to calculate the DR stimulation threshold. The results are then postprocessed and the following parameters are calculated to compare the quantitive results:

- **Perception threshold (PT):** defined as the lowest voltage needed to activate the first DC 12.8-μm (PT$_{DC}$) or DR 15-μm diameter (PT$_{DR}$) nerve fiber. This value is the electrode voltage and is expressed as the voltage programmed in a pole (the leading edge of the stimulation pulse, in V).
- **Discomfort threshold (DT):** this is the clinical value that produces painful paresthesia. In the volume conductor models, DT is the ratio between the perception threshold and discomfort obtained from the real patients per PT and
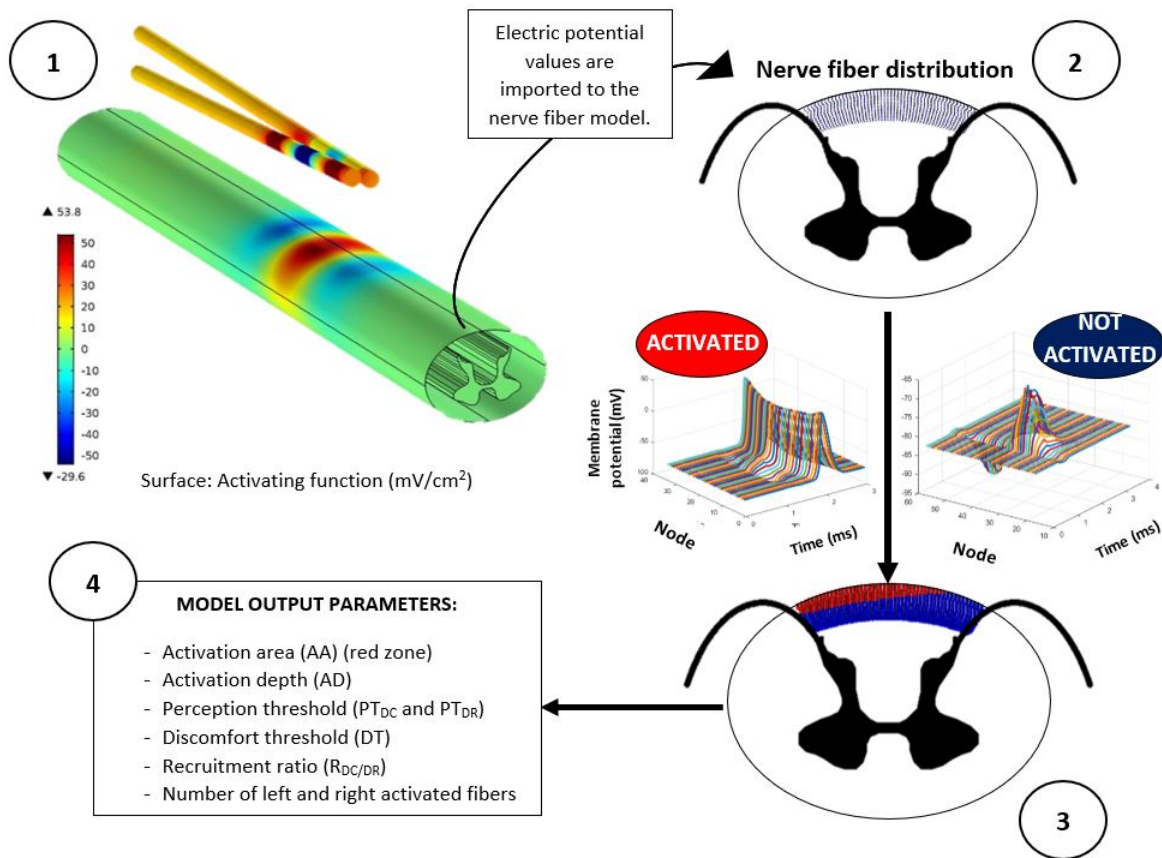
Figure 4: **Scheme of the simulation procedure in the generalized spinal cord model.** Step 1 (top left): simulation of the electric field and representation of the activating function on the surface of the spinal cord (white matter). Red indicates zones with high electric potential variation and thus where neural activation is most likely. Step 2 (top right): axial view of the spinal cord and transversal projection of the nerve fibers to show nerve fiber distribution and DR fibers locations. The electrical values at each node of Ranvier and fiber internodes for both DC and DR nerve fibers are imported to the nerve fiber model as an input parameter. Step 3 (bottom right): activated DC nerve fibers shown in red (action potential propagation) and not activated DC nerve fibers shown in blue (no action potential). Step 4 (bottom left): postprocessing of the results to calculate the quantitative parameters: activation area, activation depth, perception threshold, discomfort threshold and recruitment ratio. DC: dorsal column, DR: dorsal roots.

thus may be the ratio value per PT_{DC} or the ratio value per PT_{DR}, since both neural structures could be involved in PT [45].

- **Recruitment ratio ($R_{DC/DR}$):** the ratio between PT_{DC} and PT_{DR}, which indicates the nerve fibers most likely to be activated first: DR (values equal to or higher than 1) or DC nerve fibers (lower than 1).

- **Activating area (AA):** defined as the maximum transversal area of the DCs within which DC nerve fibers are activated at DT.

- **Activating depth (AD):** the maximum cross-sectional depth of the DCs within which DC nerve fibers are activated at DT.

- **Number of left and right activated fibers**: defined as the transverse (left or right) cross-sectional area that is stimulated (in μm^2) per density of 12.8-μm fibers in the DC ($0.11 \cdot 10^{-3}(\mu m^2)^{-1}$, according to Feirabend et al. [38]). It represents the number of fibers that would be activated.

This simulation procedure was used for both the generalized and patient-specific model simulations. All the simulations were performed with a rectangular monophasic pulse stimulus of 300 μs pulse width, which is similar to the clinical stimulation scenario that includes a lower amplitude passive charge recovery phase [46]. Although the frequency is set to 50 Hz clinically, in the simulations we apply just one pulse, for nerve fibers are activated at each pulse in tonic stimulation [46]. This assumption considers electrical stimulation as a quasi-static phenomenon, which is valid for frequencies up to 10 kHz [47].

3. Results

3.1. Clinical retrospective proof of concept

3.1.1. Patient 1 The first patient in the study was a 47-year-old woman diagnosed with failed back surgery syndrome who had reported chronic pain in both left lower limb and left lower back. We found guarded cathode (GC) ((+)(−)(+)) and transverse guarded cathode (TGC) ((+)(−)(+) in one electrode and a (+) located next to (−) using the other electrode) polarities which produced paresthesia coverage in her pain dermatomes. As the patient reported an undesired pleasant tingling sensation in the right lower limb with GC polarity, TGC was used to manage her chronic pain. We collected the values of the stimulation parameters (PT and DT) with the patient standing, as shown in Table 2. PT was obtained when the patient started feeling a slight tingling sensation and DT when the stimulation amplitude was raised and the patient reported an unpleasant sensation. Figure 5 shows the induced paresthesia coverage in the front and back body and the programmed polarity.

Using the patient-specific and generalized models we calculated the stimulation parameters for GC (5(+), 6(−), 7(+) (see figure 5a)) stimulation, shown in Table 2. Figure 6c reveals that there are more activated nerve fibers on the left side than on the right of the DCs in the generalized model. The same effect was obtained in the patient-specific model (see figure 6a) but fewer nerve fibers would be activated on the right side of the DC (34 nerve fibers versus 55 nerve fibers activated in the generalized model). Moreover, the opposite effect is obtained on the left, i.e. the number of fibers
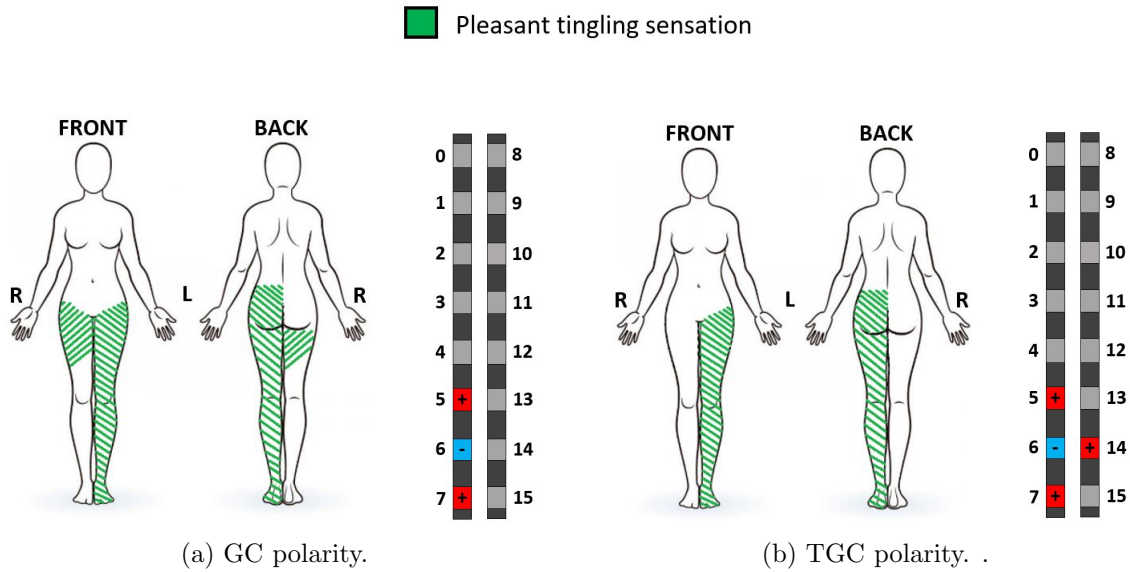
(a) GC polarity.   (b) TGC polarity. .

Figure 5: **Paresthesia coverage of patient 1.** GC: guarded cathode; TGC: transverse guarded cathode. The striped green zones represent the zones where the patient feels a pleasant tingling sensation during stimulation. Left electrode: from pole 0 to pole 7; right electrode: from pole 8 to pole 15. Vertebral level stimulated in both programs: T9. R: right; L: left.

that would be activated is 17.21% higher than in the generalized model (143 versus 122). As for the stimulation parameters, we can see that AA does not change (1.62 mm^2 for both models) and AD is 5.3% lower in the generalized than in the patient-specific model (500 versus 528 μm, respectively). On the other hand, PT$_{DC}$ is 190%

Table 2: : **Evaluation parameters obtained from the real patient 1, the generalized spinal cord model and the patient-specific spinal cord model. PT$_{DC}$: perception threshold in DC; PT$_{DR}$: perception threshold in DR; DT: discomfort threshold; R$_{DC/DR}$: recruitment ratio; AA: activating area; AD: activating depth.**

Source	PT$_{DC}$ (V)	PT$_{DR}$ (V)	DT (V)	R$_{DC/DR}$	AA (mm^2)	AD (μm)
Guarded cathode polarity						
Real patient 1	1.4	-	1.9	-	-	-
Generalized model	3.8	11.2	5.16	0.34	1.62	500
Patient-specific model	1.31	4.16	1.78	0.314	1.62	528
Transverse guarded cathode polarity						
Real patient 1	1.6	-	2.2	-	-	-
Generalized model	4.28	9.1	5.9	0.47	1.46	450
Patient-specific model	1.52	3.2	2.1	0.475	1.32	391

(a) Patient-specific model. GC polarity.

(b) Patient-specific model. TGC polarity.

(c) Generalized model. GC polarity.
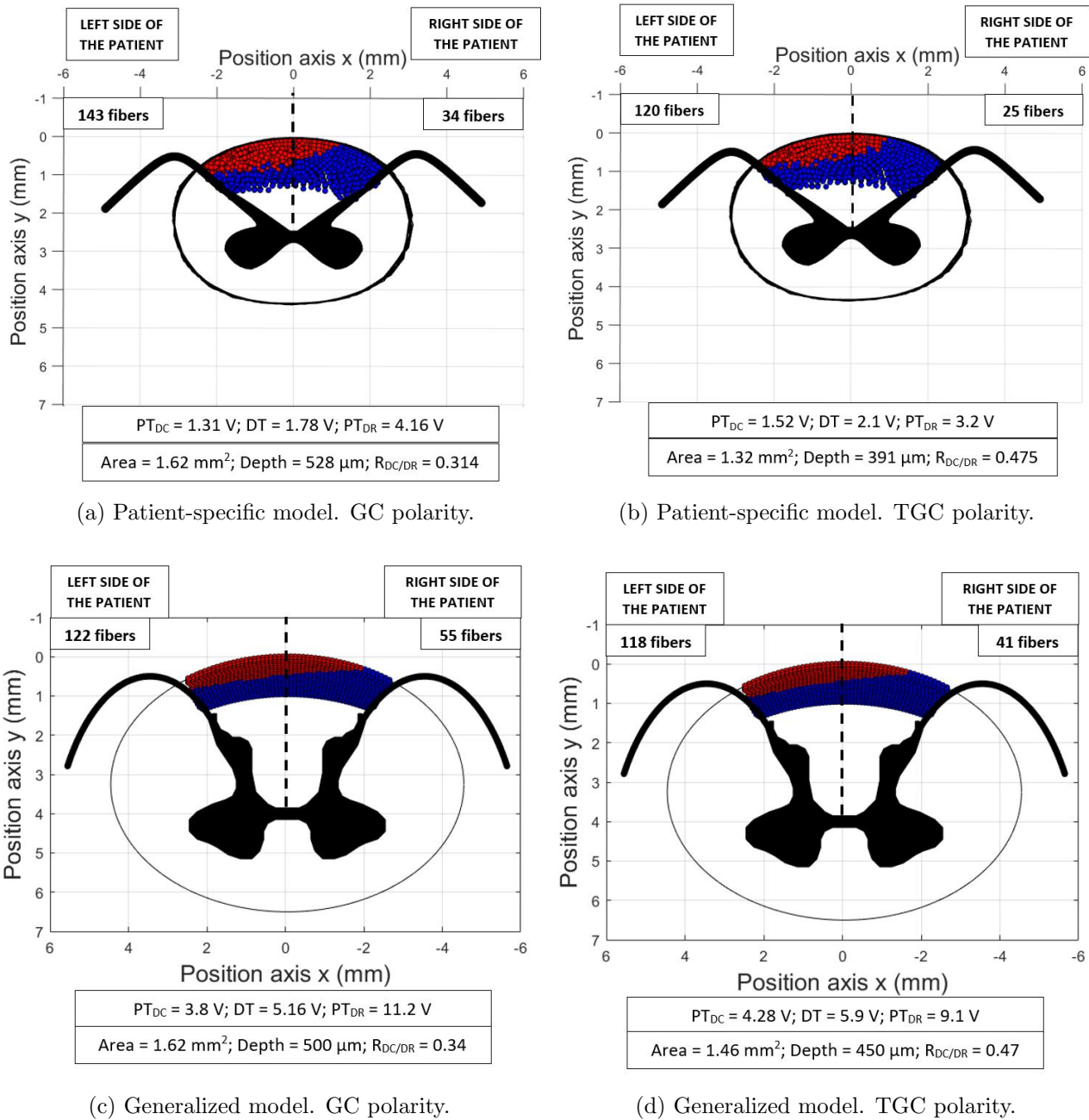

(d) Generalized model. TGC polarity.

Figure 6: **Evaluation parameter prediction in TGC and GC polarities.** Red points represent activated nerve fibers. Blue points are not activated nerve fibers. White areas are zones with no nerve fibers considered. Stimulus applied: a rectangular pulse of 300 μs duration with an electrical strength of 1.357 PT for GC polarity and 1.375 PT for TGC in V. Dashed line represents the central line of the spinal cord. TGC: transverse guarded cathode; GC: guarded cathode; PT: perception threshold.

higher using the generalized model (3.8 V versus 1.31 V) and so DT is 189.9% and PT_{DR} is 169.2% higher than the values obtained with the patient-specific model (5.16

V versus 1.78 V and 11.2 V versus 4.16 V, respectively). $R_{DC/DR}$ prediction is similar in both models, more specifically 7.94% higher in the generalized model (0.34 versus 0.314).

The results of the TGC (5(+), 6(−), 7(+) and 14(+) (see figure 5b)) polarity stimulation are shown in figures 6b and 6d. There are more activated nerve fibers on the left than the right side. Both the generalized and the patient-specific spinal cord model obtained the same results as GC polarity, i.e. more nerve fibers would be activated on the right in the generalized model (41 versus 25 nerve fibers). There is a similar difference in the stimulation parameters: AA and AD are 10.6% and 13.06% higher in the generalized than in the patient-specific model (1.46 versus 1.32 mm^2 and 450 versus 391 μm), PT_{DC} is 181.57% higher using the generalized model, DT is 180.9% and PT_{DR} is 184.4% higher than those obtained using the patient-specific model. $R_{DC/DR}$ prediction is also similar but in this case is 1.06% lower in the generalized model (0.47 versus 0.475). However, unlike GC, TGC polarity produces a neural activation displacement in the site opposite to where the transversal anode is programmed, reducing the number of activated nerve fibers by 26.47% on the right side of the DC (34 versus 25 nerve fibers using GC and TGC polarities in the patient-specific model, respectively).

Table 2 shows the patient's evaluation parameters obtained from the generalized model and the patient-specific model. Although AA, AD and $R_{DC/DR}$ are very similar in both models, the latter predicts the stimulation thresholds more accurately. For example, for TGC polarity, the real patient reported a PT_{DC} of 1.6 V. With the patient-specific model, the PT_{DC} value is only 5% lower than the one from the real patient while it is 167.5% higher in the generalized model. The same effect occurs for DT and PT_{DR} values prediction in GC and TGC polarities.

3.1.2. Patient 2 The second patient in the study was a 54-year-old woman diagnosed with failed back surgery syndrome who had reported chronic pain in the center-right lower back. Three programs were tested to cover her painful dermatomes. Only one of the programs (program 2) produced paresthesia coverage in the center lower back, which was used to manage her chronic pain. Figure 7 shows the induced paresthesia coverage in the front and the back body and the programmed polarity. As in patient 1, we collected the values of the stimulation parameters (PT and DT) for the three programs with the patient standing, as shown in Table 3.

The stimulation parameters were calculated for the three programs by using the patient-specific model and three versions of the generalized model (one for each vertebral level stimulated with the programs: T8, T9 and T10). The results are shown in Table 3.

In program 1, PT_{DC}, PT_{DR} and DT are higher in the patient-specific than in the generalized model (3.9%, 8.7%, and 8.65% higher, respectively). In both models, the
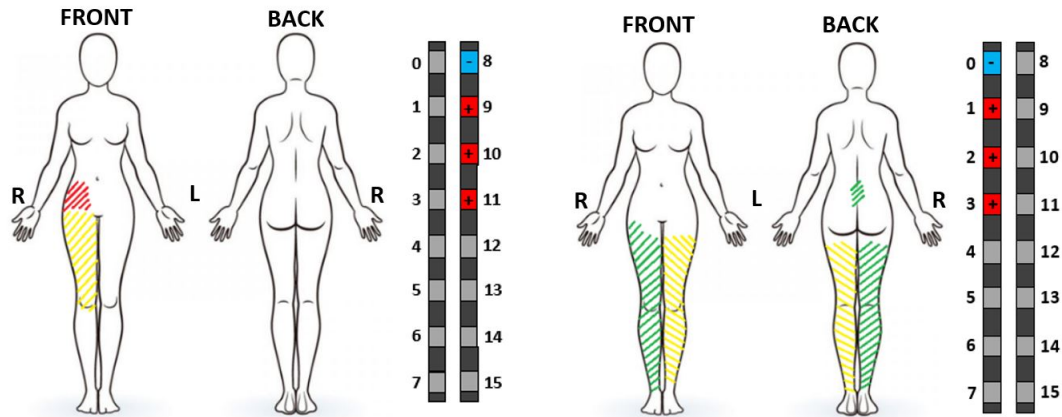
(a) Program 1. Vertebral level stimulated: T8.

(b) Program 2. Vertebral level stimulated: T9.
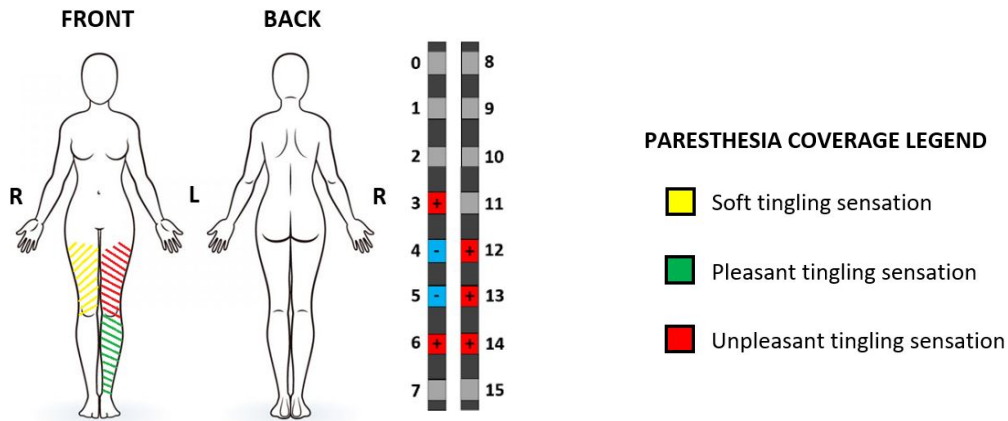
(c) Program 3. Vertebral level stimulated: T10.

(d) Paresthesia coverage legend.

Figure 7: **Paresthesia coverage of patient 2.** The striped zones represent the anatomic location where the patient feels a tingling sensation during stimulation. Soft tingling (yellow): a slight tingling that is felt like the initial sensation that is produced when the perception threshold is achieved. Pleasant tingling (green): strong and comfortable sensation produced at a stimulus amplitude that is just below the discomfort threshold. Unpleasant tingling (red): discomfortable and painful sensation that is produced at (or above) the discomfort threshold. Left electrode: from pole 0 to pole 7; right electrode: from pole 8 to pole 15. R: right; L: left.

stimulation starts at the DR. However, $R_{DC/DR}$ is 4.5% lower in the patient-specific model. This difference affects AA and AD predictions, which are higher in the patient-specific model (0.346 versus 0.055 mm^2 and 362.76 versus 50 μm, respectively). As shown in figure 8, no left fibers would be activated in both models, which is in agreement with the paresthesia coverage clinical data (see figure 7a), since no tingling sensation is felt in the left side. Nevertheless, in the patient-specific model more right fibers would be

activated than in the generalized model (33 versus 6, respectively).

In program 2, PT_{DC}, PT_{DR}, and DT are lower in the patient-specific than in the generalized model (16.1%, 5.2%, and 11.4% lower, respectively). Instead, $R_{DC/DR}$ is higher in the generalized model (1.06 versus 0.934), so the stimulation starts at the DR, while it does at the DC in the patient-specific model. However, although AA is higher in the generalized model (0.76 versus 0.56 mm^2), AD is lower than in the patient-specific model (300 versus 423.74 μm, respectively). Figure 8 shows that more right than left fibers would be activated in the patient-specific model (38 on the right versus 21 on the left). Instead, the opposite effect is obtained in the generalized model, i.e. more left fibers would be activated (52 on the left versus 32 on the right). According to paresthesia coverage clinical data (see figure 7b), more tingling sensation is felt in the right lower limb. Therefore, the patient-specific model results are in agreement with the clinical data.

In program 3, the stimulation parameters values (PT_{DC}, PT_{DR}, and DT) are similar in both models. While PT_{DC} is 7.14% higher in the patient-specific model, PT_{DR} is 8.2% lower. $R_{DC/DR}$ is lower than 1 in the generalized model (0.918), so the stimulation starts at the DC. Conversely, in the patient-specific model, $R_{DC/DR}$ is higher than 1 (1.07), so the activation is first produced at DR fibers. Consequently, AA and AD are higher in the generalized model (1.29 versus 0.4 mm^2 and 450 versus 312.17 μm, respectively).

Table 3: **Evaluation parameters obtained from the real patient 2, the generalized spinal cord model and the patient-specific spinal cord model. PT_{DC}: perception threshold in DC; PT_{DR}: perception threshold in DR; DT: discomfort threshold; $R_{DC/DR}$: recruitment ratio; AA: activating area; AD: activating depth.**

| Source	PT_{DC} (V)	PT_{DR} (V)	DT (V)	$R_{DC/DR}$	AA (mm^2)	AD (μm)
Program 1. T8 vertebral level						
Real patient 2	6	-	6.8	-	-	-
Generalized model	5.1	4.6	5.2	1.11	0.055	50
Patient-specific model	5.3	5	5.65	1.06	0.307	362.76
Program 2. T9 vertebral level						
Real patient 2	4.5	-	5.6	-	-	-
Generalized model	5.08	4.81	5.96	1.06	0.76	300
Patient-specific model	4.26	4.56	5.28	0.934	0.56	423.74
Program 3. T10 vertebral level						
Real patient 2	3.6	-	4.4	-	-	-
Generalized model	3.36	3.66	4.1	0.918	1.29	450
Patient-specific model	3.6	3.36	4.1	1.07	0.4	312.17
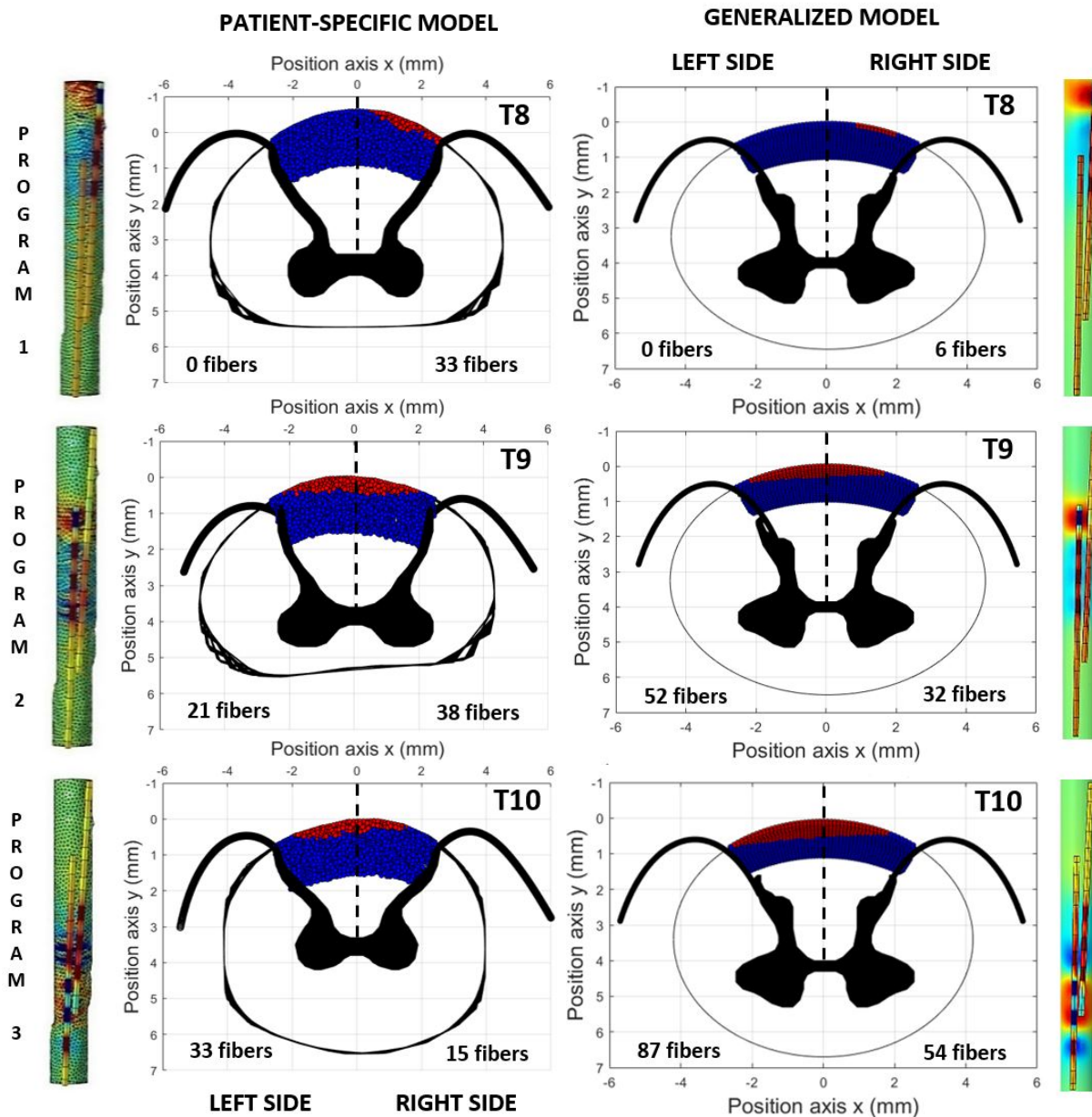
Figure 8: **Evaluation parameter prediction for patient 2.** Red points represent activated nerve fibers. Blue points are not activated nerve fibers. White areas are zones with no nerve fibers considered. Stimulus applied: a rectangular monophasic pulse of 300 μs duration with an electrical strength of 1.13 PT for program 1 in V; 1.24 PT for program 2; and 1.22 PT for program 3. Dashed line represents the central line of the spinal cord.

In terms of paresthesia coverage, the patient reported unpleasant sensation in the anterior lower left thigh, and a soft sensation in the anterior lower right thigh (see figure 7c). Both models predict right fibers activation (see figure 8), which is in agreement with the clinical data. However, in the patient-specific model lower right fibers would

be activated than in the generalized model (15 versus 54, respectively). And the same occurs on the left side, more left fibers would be activated in the generalized model (87 versus 33 in the patient-specific model).

As shown in Table 3, the patient-specific model predicts PT_{DC} and DT values that are closer to clinical data. In program 1, PT_{DC} and DT are 11.67% and 16.91% lower than in the real patient (5.3 versus 6 V and 5.65 versus 6.8 V, respectively), while they are 15% and 23.53% lower in the generalized model (5.1 versus 6 V and 5.2 versus 6.8 V). In program 2, PT_{DC} and DT are 5.3% and 5.71% lower than the clinical values. Conversely, the generalized model presents PT_{DC} and DT values that are 12.88% and 6.43% higher than the clinical data. In program 3, the generalized model PT_{DC} value is 6.67% lower than the value of the real patient (3.36 versus 3.6 V), while the patient-specific model PT_{DC} is in agreement with the clinical data. As for DT value, both the generalized and patient-specific models are 6.81% lower than the clinical value (4.1 versus 4.4 V, respectively).

3.2. Sensitivity analysis

As shown in previous studies [48], the stimulation parameters (PT_{DC}, PT_{DR}, AA and AD) are all influenced by the geometry of the spinal cord and the electrode position in the epidural space. Therefore, a sensitivity analysis was conducted with the generalized model to identify the geometric parameters of the spinal cord that had the greatest effect on the stimulation parameters. The analysis examined the relative changes in PT_{DC}, PT_{DR}, AA and AD that resulted from varying the dorsal CSF (dCSF) thickness and the CSF diameter in their physiological range for T9 vertebral level (4-6 mm and 12-16 mm, respectively) [17]. Moreover, the effect of electrode-dura mater distance (D_{e-d}) was also included in the analysis.

Figure 9 reveals that PT_{DC} and PT_{DR} are most sensitive to D_{e-d}. The increase of D_{e-d} causes the increase of PT_{DC} and PT_{DR}. Changes in dCSF thickness also causes the increase of both PT_{DC} and PT_{DR}. But, while the 1 mm increase in D_{e-d} increases PT_{DC} by 76.1% and PT_{DR} by 54.1%, the 1 mm increase in dCSF increases PT_{DC} by 50.8% and PT_{DR} by 26.6%. Variations in CSF diameter also produces changes in the stimulation thresholds. For instance, increasing 1 mm of CSF diameter causes 2.1% change in PT_{DC} and 5.9% change in PT_{DR}.

AA is also shown to be sensitive to D_{e-d}, dCSF, and CSF diameter. Variations in D_{e-d} and dCSF causes the increase of AA. In this case, AA is more sensitive to dCSF, since the 1 mm increase of D_{e-d} increases AA by 18.7%, while 1 mm increase of dCSF increases AA by 26.1%. However, opposite change is caused when CSF diameter increases. Increasing 1 mm of CSF diameter causes 2.23% reduction in AA.
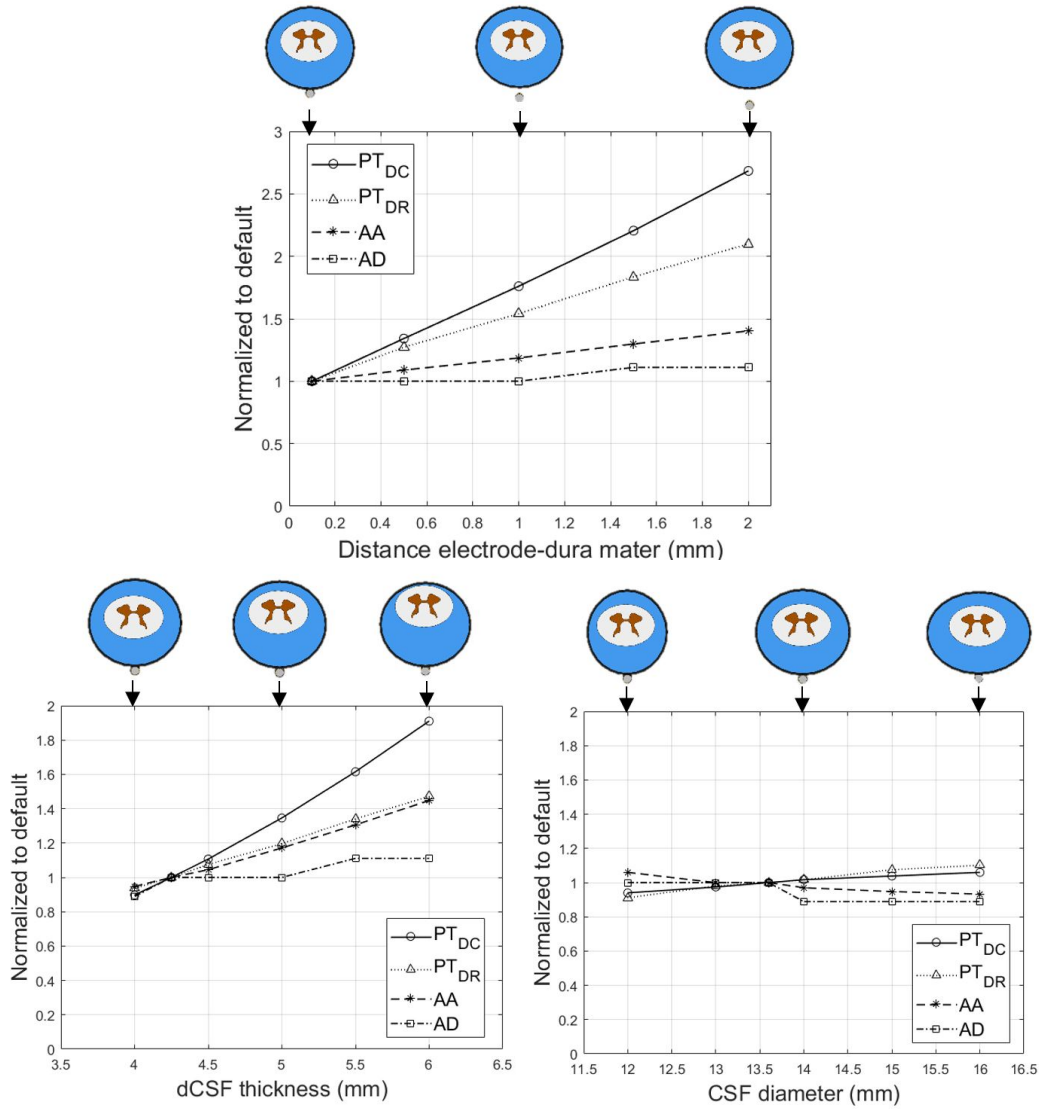
Figure 9: **Sensitivity analysis.** Sensitivity of perception threshold on DC (PT$_{DC}$), perception threshold on DR (PT$_{Dr}$), activating area (AA), and activating depth (AD) to variations in geometric parameters of the spinal cord and electrode-dura mater distance (D$_{e-d}$). All parameter values are expressed as multiples of default parameter value. All PT$_{DC}$, PT$_{DR}$, AA, and AD are normalized to their respective values obtained with default parameters. Default parameters: dCSF: 4.25 mm; CSF diameter: 13.6 mm; D$_{e-d}$: 0.1 mm; vertebral level: T9. Stimulation parameters applied: rectangular monophasic pulse; bipolar configuration; pulse width: 300 μs.

Variations in D$_{e-d}$ and dCSF cause similar changes in AD, i.e. a 11% maximum increase in AD is obtained when D$_{e-d}$ and dCSF increase to their maximum values (2 and 6 mm, respectively). The opposite effect is caused when CSF diameter increases to its maximum value (16 mm), i.e. AD is reduced to a maximum of 11%.

3.3. Pre-implantation selection of the electrode polarity. Clinical application

Selecting stimulation parameters before SCS surgery could be a future application of a 3D patient-specific model. For this study we used the patient-specific model of the patient 1.

The electrodes were located at an ideal position (epidural space over the dura mater, parallel to the white matter and 2.5 mm center-to-center separation) to maximize neural activation on the left side of the spinal cord. The electrode program used for TGC polarity simulations has been experimentally shown to be the best to cover pain dermatomes in the real patient 1. We then simulated the effect of moving electrode polarity from the poles below to those above the electrodes (six cases shown in figure 10) to determine the electrode program most likely to cover the patient's painful dermatomes.

As the white matter geometry changes at each slice, as shown in figure 10, the fibers to be activated depend on the stimulation poles selected and the electrode location. The evaluation parameters were calculated to find the differences for the six cases considered (see Table 4).

Table 4: **Evaluation parameters obtained from the patient-specific spinal cord model. PT_{DC}: perception threshold in DC; PT_{DR}: perception threshold in DR; DT: discomfort threshold; $R_{DC/DR}$: recruitment ratio; AA: activating area; AD: activating depth.**

Cases	PT_{DC} (V)	PT_{DR} (V)	DT (V)	$R_{DC/DR}$	AA (mm^2)	AD (μm)	Left fibers	Right fibers
Parallel electrodes								
Case 1. 5(+)6(−)7(+) and 14(+)	1.33	4.54	1.86	0.292	1.2	398.2	120	11
Case 2. 4(+)5(−)6(+) and 13(+)	1.06	3.86	1.49	0.275	1.77	502.1	171	23
Case 3. 3(+)4(−)5(+) and 12(+)	1.03	3.33	1.44	0.31	1.52	500	163	4
Case 4. 2(+)3(−)4(+) and 11(+)	1.08	3.21	1.51	0.335	1.41	457.8	213	2
Case 5. 1(+)2(−)3(+) and 10(+)	1.16	1.96	1.62	0.592	1.18	456	119	11
Case 6. 0(+)1(−)2(+) and 9(+)	1.31	3.57	1.83	0.367	1.46	532	152	8
Parallel electrodes with offset								
Case 2. 4(+)5(−)6(+) and 13(+)	0.86	2.87	1.2	0.3	1.71	462.6	129	58

(a) Case 1. 5(+),6(−),7(+) and 14(+).

(b) Case 2. 4(+),5(−),6(+) and 13(+).

(c) Case 3. 3(+),4(−),5(+) and 12(+).

(d) Case 4. 2(+),3(−),4(+) and 11(+).

(e) Case 5. 1(+),2(−),3(+) and 10(+).
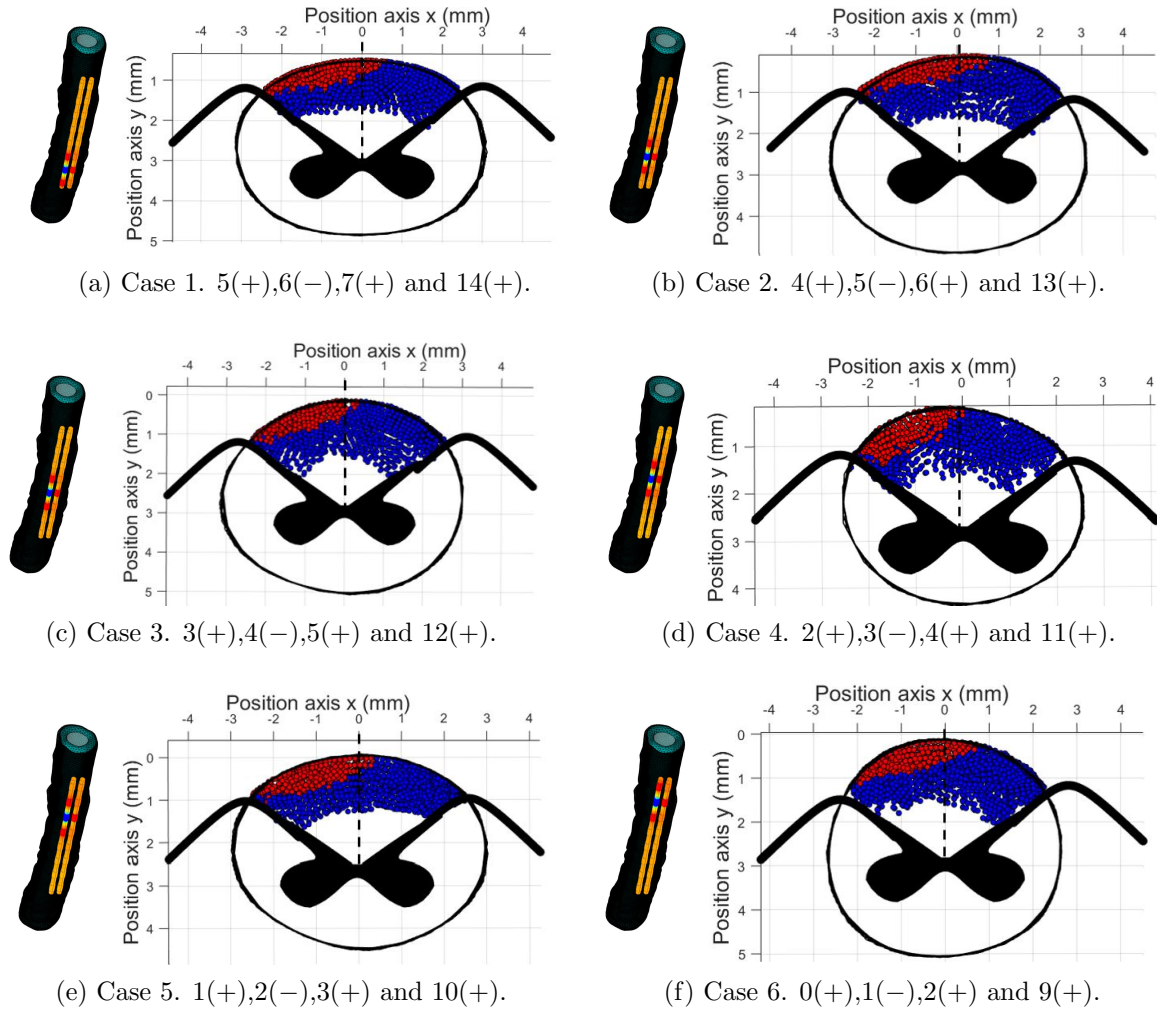

(f) Case 6. 0(+),1(−),2(+) and 9(+).

Figure 10: **Activation area and depth at ideal electrode position in the 3D patient-specific model of patient 1. TGC polarity.** Red points represent activated nerve fibers, blue points not activated nerve fibers. White area represents zones with no nerve fibers considered. Stimulus applied: a rectangular monophasic pulse of 300 μs duration with an electrical strength of 1.4 PT in V. Vertebral bodies and fat tissues are hidden to highlight electrode polarity. Red poles are anodes and blue poles cathodes. Dashed line is the central line of the spinal cord. PT: perception threshold. Programmed poles for each case: Case 1: 5(+)6(−)7(+) and 14(+); Case 2: 4(+)5(−)6(+) and 13(+); Case 3: 3(+)4(−)5(+) and 12(+); Case 4: 2(+)3(−)4(+) and 11(+); Case 5: 1(+)2(−)3(+) and 10(+); Case 6: 0(+)1(−)2(+) and 9(+).

In general, Case 4 (figure 10d) maximizes the number of left-activated nerve fibers (213 versus 2 right-activated fibers), while Case 2 (figure 10b) activates more right fibers (23), maximizes AA (1.77 mm^2) and minimizes $R_{DC/DR}$ (0.275). In terms of PT_{DC}, Cases 2 (figure 10b), 3 (figure 10c) and 4 (figure 10d) present the lowest values (1.06, 1.03 and 1.08, respectively), since in these cases the electrodes are closer to the dura mater, due

to the geometry of the patient's spinal cord. Instead, Cases 1 (figure 10a), 5 (figure 10e) and 6 (figure 10f) need higher PT_{DC} values to activate the nerve fibers (between 12-29% higher than Cases 2, 3 and 4). AD is also affected, being higher in Case 6 (532 μm) and lower in Case 1 (398.2 μm). In Cases 2 and 3, AD is about 500 μm, while it is about 10% lower in Cases 4 and 5 (457.8 μm and 456 μm, respectively).

3.4. Effect of electrode offset

The effect of electrode offset on neural activation was studied by using the patient-specific model of patient 1. Implanted electrodes may be either perfectly parallel, i.e. with the poles of the two electrodes facing each other, or one can be offset to avoid them facing each other.

We compared AA and AD with parallel electrodes against parallel electrodes with a vertical offset of 3.5 mm, i.e. interspersed poles. As Case 2 would activate more right nerve fibers, this case was used to study the effect of electrode offset.

Figure 11 shows that the effect of electrode offset is the loss of the electric field displacement achieved with TGC polarity. The evaluation parameter values are also shown in Table 4. When TGC is applied with the electrodes in parallel, the number of left-activated nerve fibers is 32.56% higher than with electrode offset (171 versus 129 nerve fibers) and the number of right-activated nerve fibers increases by 52.17% with offset electrodes (23 versus 58, respectively). In terms of AA and AD, offset electrodes also reduce these parameters (1.77 mm^2 versus 1.71 mm^2 and 502.1 μm versus 462.6 μm, respectively). $R_{DC/DR}$ is about 9% higher than paralleled electrodes (0.275 versus 0.3). However, PT_{DC} is about 20% lower with offset (1.06 V versus 0.86 V) since the first activated nerve fiber is closer to the electrode and there is no electric field displacement.

4. Discussion

This paper describes the first SCS patient-specific model that includes the spinal cord geometry variation along three vertebral levels (from T8 to T10), which solves one of the main limitations reported by Lempka *et al.*, i.e. the use of the same spinal cord dimensions for all the vertebral levels considered [20]. This is an important point as it is known that the different levels have different dimensions, and this could play an important role when programming or implanting electrodes. As an innovation, we include the whole spinal cord geometry taken from 3T MR images of the patient, except the dura mater, whose thickness was based on measurements from human cadavers [29, 30]. We also include the exact geometry of the patient's vertebral bodies. According to Zander et al. [31], albeit vertebral bone could be simplified as a cylindrical domain, the inclusion of detailed 3D anatomical vertebrae is fundamental to consider potential threshold changes. Vertebral body anatomy determines the geometry of the epidural

(a) Parallel electrodes
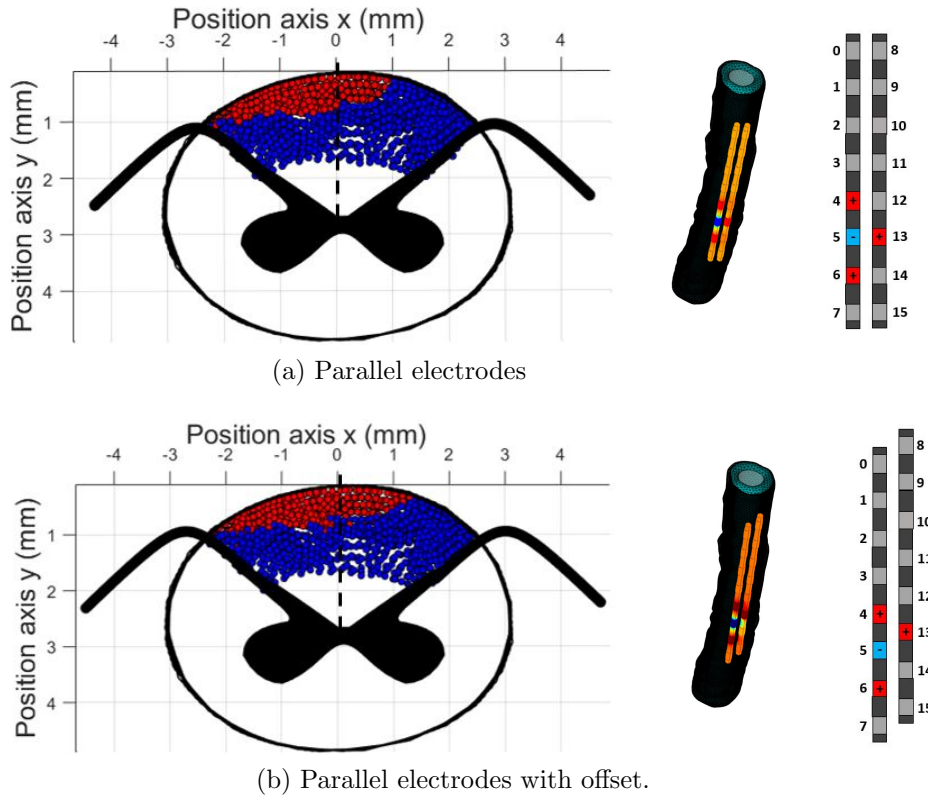

(b) Parallel electrodes with offset.

Figure 11: **Electrode offset effect on activation area and depth. TGC polarity.**
Red points represent activated and blue not activated nerve fibers. White area represents
zones with no nerve fibers considered. Stimulus applied: a rectangular monophasic
pulse 300 μs duration with an electrical strength of 1.4 PT in V. Programmed poles:
4(+),5(−),6(+) and 14(+). Red poles are anodes and blue poles cathodes. Vertebral
bodies and fat tissues are hidden to highlight electrode polarity. Offset is generated by
raising the right electrode position on the y axis by 3.5 mm. Dashed line is the central
line of the spinal cord. PT: perception threshold.

space at the different vertebral levels. Therefore, the relative position of the stimulating
electrodes is included in the patient-specific model, and potential threshold changes can
be considered.

One of the main goals of this study was to examine the significance of a patient-
specific model over a generalized model. Our results show that the patient-specific model
stimulation threshold prediction fits better with the clinical data than the generalized
model, which is in agreement with the results obtained by Lempka *et al.* [20]. In
patient 1, the generalized model predicted higher thresholds for PT_{DC}, and DT (see
Table 2). On the base of the sensitivity analysis results, the stimulation parameters
are strongly sensitive to electrode position (D_{e-d}), and dCSF thickness (see figure 9).
These geometrical parameters are significantly lower in the patient-specific than in the

generalized model in patient 1 (see Supplementary information for the geometry data, Section 1), which explains the difference observed in thresholds prediction. In patient 2, the generalized model predicted lower thresholds in programs 1 and 3, and higher thresholds in program 2 (see Table 3). In this case, $D_{e\text{-}d}$ and dCSF thickness are similar in both the patient-specific and the generalized model (see Supplementary information for the geometry data, Section 1). Hence, the difference in thresholds prediction is not as marked as in patient 1. However, the patient-specific model also produced estimates of PT_{DC} and DT that were more consistent with the clinical measurements.

We also simulated the neural activation predictions at clinical DT in both patients. In patient 1, PT_{DR} is higher than PT_{DC} in both models (see Table 2). Thus, the stimulation patterns are similar, i.e. there are more left-activated fibers. However, the generalized model predicted more right-activated fibers than the patient-specific model (see figure 6). Given that patient 1 reported a slight tingling sensation in the right thigh with GC polarity, in addition to no tingling sensation in the right side with TGC polarity, the patient-specific model produced axonal activation that is more consistent to clinical results. This outcome suggests that the laterality of the neural activation depends on the relative position of the electrodes, and the spinal cord offset within the spinal canal. Moreover, we compared the effect of TGC versus GC polarity in this patient. The results demonstrated that transverse polarity displaced the sweet spot (the first activated nerve fiber), which is in concordance with a previous study [49], and the clinical results (see figure 5). In patient 2, the stimulation pattern changes at each program. For instance, unlike the patient-specific model, the generalized model predicted DR stimulation and more left-activated fibers in program 2 (see Table 3 and figure 8), which was not in agreement with the clinical data (see figure 7b). From the sensitivity analysis results, PT_{DR} was more sensitive to CSF diameter than PT_{DC} (see figure 9). Hence, variations in the $R_{DC/DR}$ produced significant changes in the stimulation patterns. These results suggest that the inclusion of the patient's spinal cord anatomy is pivotal for predicting the effect of SCS accurately.

To examine the capability of the patient-specific model, we performed a clinical application for electrode program planning. In this case we used the patient-specific model from patient 1, who reported chronic pain in the left lower limb and left lower back. According to Taghva et al. [50], T9 and T10 are the most likely vertebral areas to cover most areas of the body. However, T8 is more likely to cover buttocks, back and thigh, and less likely to cover leg and foot. As T9 is less likely to cover the anterior leg and T10 is not likely to cover the low back above the waist, for this patient, in order to ensure paresthesia coverage in the left lower limb and back, the electrodes were located ideally across the T8 and T9 vertebral levels (5 poles per lead in T9 and 3 poles per lead in T8). Eight-pole percutaneous electrodes allowed us to stimulate the vertebral level using different programs and poles. This is useful because, when some electrode poles fail, electrode replacement surgery can be avoided by programming the working poles. The outcome of the use case (see figure 10) shows that the programmed poles

used in Case 4 (see figure 10d) are the best to ensure paresthesia coverage on the left side of the body.

However, if non-targeted dermatomes are stimulated with this program or the stimulation is painful (since these poles in the patient-specific model are between T8 and T9), the programmed poles used in Case 3 (see figure 10c) or Case 1 (see figure 10a) would also allow us to maximize neural activation on the left side, and as these poles are at T9 they are likely to cover the patient's painful dermatomes. This use case therefore shows that it is possible to determine the poles that should be programmed first to maximize paresthesia coverage using a patient-specific spinal cord model.

We also studied the effect of offset electrodes on neural activation using the patient-specific model from patient 1. Based on our results, with TGC polarity the offset reduces the capability of TGC polarity to activate the more lateral nerve fibers (see figure 11). As it was important for the patient studied to center activation on the left side of the DCs, electrode offset would not be beneficial since it would be more difficult to focus paresthesia coverage on the painful left dermatomes. In the event of non-paresthesia-based stimulation, leads with a staggered offset placement is used to cover the target areas in a contiguous fashion [51, 52]. However, our results suggest that aligned electrodes should be implanted in tonic stimulation, for this leads placement could enhance right or left dermatomes selection, contributing to a better patient's paresthesia coverage.

The results of this study exhibited excellent agreement between the 3D patient-specific model and clinical measurements, however the study had several limitations. This study was a proof-of-concept performed with two patients within which the geometrical spinal cord parameters that most affect SCS effect were identified. To obtain statistically significant results, a cohort of patients should be included in future studies. More electrode configurations should be tested along the three vertebral levels (from T8 to T10) to validate clinically the patient-specific model.

In terms of nerve fiber distribution, both the generalized and the patient-specific model include overpopulation of 12.8-μm nerve fiber diameter in the DC. According to Feirabend et al. [38], nerve fiber diameters higher than 11.5 μm are sparse in the DC. But it is well-known that large nerve fibers show lower stimulation thresholds than small nerve fibers [20, 22, 53]. Assuming that PT is obtained when the largest nerve fiber is activated in the DC, we only considered a 12.8-μm nerve fiber diameter and overpopulated the DC in order to minimize the effect of the location of these fibers on the calculated thresholds. However, as previous studies show [12, 20, 41], the inclusion of different nerve fiber diameters is useful, notably when the aim of the study is related to the mechanisms of action or the effect of a stimulation parameter on neural activation. On the other hand, recent studies assume that 10% of fibers are activated at the perception threshold instead of a single nerve fiber [20, 54, 55]. According to Anaya et al. [55], although computational modeling results showed well-matching with

the clinical data, there is still no relationship established between clinical measurements of PT or DT and the corresponding degrees of DC neural activation. This limitation could affect the PT values obtained in this study, which would explain the slightly lower thresholds obtained with the patient-specific model compared to the clinical data (see Table 2 and Table 3).

The generalized model is based on measurements from MRI acquisitions that were obtained with the patient in prone position. On the contrary, the MRI scans for the patient-specific model were obtained with the patient in supine position. The patient posture during X-ray scans was prone. Furthermore, we collected the stimulation thresholds (PT_{DC} and DT) with the patient standing. Postural changes produce dCSF thickness variations, generating stimulation thresholds changes, as shown in previous studies [4, 21]. Thus, the patient position could explain the differences observed between the models' stimulation thresholds prediction and the clinical measurements.

The grey matter is not included in the patient-specific volume conductor model. As the electric field does not seem to be affected by the grey matter [56] it was not included to reduce the computational cost. However, future patient-specific models should include this structure since recent SCS action mechanisms are focused on the dorsal horns of the grey matter [57].

Percutaneous electrodes are flexible and can be curved when implanted. However, in the SCS model, the electrodes are modeled as rigid solids so that in some cases it would be difficult to simulate the effect of the real electrode positions or to find the best electrode location. In order to perform more realistic simulations, future SCS models should therefore include flexible percutaneous electrodes.

After electrodes implantation, blood depositions and fibrin are produced on the surroundings of the leads [58]. The encapsulation layer domain considered in the models of this study did not take into consideration these tissue heterogeneities. According to Arle et al. [24], fibrosis affects both the neural activation pattern and the stimulation thresholds. Hence, the inclusion of the tissue heterogeneities would improve the accuracy of the SCS effect prediction.

We also performed a clinical application to predict electrode polarity before the SCS implant. The lack of a somatotopic map of the spinal cord at each vertebral level, in addition to the high variability in lead placement during the implant, makes it very difficult to place the leads ideally. The distance between electrodes and the alignment of the leads are parameters that can be controlled during the SCS implant. Using the patient-specific model and the paresthesia coverage atlas developed by Taghva et al. [50], these parameters could be determined, in addition to the electrode polarity. This approach would enhance paresthesia coverage in the patient. However, a clinical study with a cohort of patients would be needed to validate this hypothesis clinically.

5. Conclusions

In this research work we developed a new realistic 3D patient-specific spinal cord model and studied its possible clinical application. The findings show that a 3D patient-specific model predicts stimulation parameters that better match clinical measurements than a generalized spinal cord model. Including the patient's spinal cord geometry is fundamental for accurately predicting the effect of SCS in a personalized way. The results suggest that in a clinical application patient-specific models would help to find the best electrode program to maximize paresthesia coverage in individual patients before SCS system implantation. 3D patient-specific models would therefore improve SCS therapy accuracy and optimize the stimulation parameters to maximize individual paresthesia coverage.

Acknowledgments

Ethical statement

This work was approved by the Drug Research Committee Ethics of the *Hospital Universitari i Politècnic La Fe*. All research was performed in accordance with the relevant guidelines and regulations and informed consent was obtained from the patients studied.

References

[1] A. W. Lee and J. G. Pilitsis, "Spinal cord stimulation: indications and outcomes," *Neurosurgical focus*, vol. 21, no. 6, pp. 1–6, 2006.

[2] Y. Guan, "Spinal cord stimulation: neurophysiological and neurochemical mechanisms of action," *Current pain and headache reports*, vol. 16, no. 3, pp. 217–225, 2012.

[3] J.-C. Kleiber, B. Marlier, M. Bannwarth, E. Theret, P. Peruzzi, and F. Litre, "Is spinal cord stimulation safe? a review of 13 years of implantations and complications," *Revue neurologique*, vol. 172, no. 11, pp. 689–695, 2016.

[4] C. H. Kim, A. W. Green, D. E. Rodgers, M. A. Issa, and M. A. Ata, "Importance of axial migration of spinal cord stimulation trial leads with position," *Pain physician*, vol. 16, no. 6, pp. E763–E768, 2013.

[5] J. Caylor, R. Reddy, S. Yin, C. Cui, M. Huang, C. Huang, R. Rao, D. G. Baker, A. Simmons, D. Souza, *et al.*, "Spinal cord stimulation in chronic pain: evidence and theory for mechanisms of action," *Bioelectronic medicine*, vol. 5, no. 1, p. 12, 2019.

[6] B. Linderoth and R. D. Foreman, "Conventional and novel spinal stimulation algorithms: hypothetical mechanisms of action and comments on outcomes," *Neuromodulation: Technology at the Neural Interface*, vol. 20, no. 6, pp. 525–533, 2017.

[7] J. Holsheimer and J. R. Buitenweg, "Bioelectrical mechanisms in spinal cord stimulation," *Neuromodulation: Technology at the Neural Interface*, vol. 18, no. 3, pp. 161–170, 2015.

[8] J. C. Oakley and J. P. Prager, "Spinal cord stimulation: mechanisms of action," *Spine*, vol. 27, no. 22, pp. 2574–2583, 2002.

[9] R. Melzack, P. D. Wall, *et al.*, "Pain mechanisms: a new theory," *Science*, vol. 150, no. 3699, pp. 971–979, 1965.

[10] L. Manola, J. Holsheimer, and P. Veltink, "Technical performance of percutaneous leads for spinal cord stimulation: a modeling study," *Neuromodulation: Technology at the Neural Interface*, vol. 8, no. 2, pp. 88–99, 2005.

[11] L. Manola, J. Holsheimer, P. H. Veltink, K. Bradley, and D. Peterson, "Theoretical investigation into longitudinal cathodal field steering in spinal cord stimulation," *Neuromodulation: Technology at the Neural Interface*, vol. 10, no. 2, pp. 120–132, 2007.

[12] D. Lee, B. Hershey, K. Bradley, and T. Yearwood, "Predicted effects of pulse width programming in spinal cord stimulation: a mathematical modeling study," *Medical & biological engineering & computing*, vol. 49, no. 7, p. 765, 2011.

[13] J. Holsheimer and W. A. Wesselink, "Effect of anode-cathode configuration on paresthesia coverage in spinal cord stimulation," *Neurosurgery*, vol. 41, no. 3, pp. 654–660, 1997.

[14] Q. Huang, H. Oya, O. E. Flouty, C. G. Reddy, M. A. Howard, G. T. Gillies, and M. Utz, "Comparison of spinal cord stimulation profiles from intra-and extradural electrode arrangements by finite element modelling," *Medical & biological engineering & computing*, vol. 52, no. 6, pp. 531–538, 2014.

[15] B. Howell, S. P. Lad, and W. M. Grill, "Evaluation of intradural stimulation efficiency and selectivity in a computational model of spinal cord stimulation," *PloS one*, vol. 9, no. 12, p. e114938, 2014.

[16] J. L. Durá, C. Solanes, J. De Andrés, and J. Saiz, "Computational study of the effect of electrode polarity on neural activation related to paresthesia coverage in spinal cord stimulation therapy," *Neuromodulation: Technology at the Neural Interface*, vol. 22, no. 3, pp. 269–279, 2019.

[17] L. Fradet, P.-J. Arnoux, J.-P. Ranjeva, Y. Petit, and V. Callot, "Morphometrics of the entire human spinal cord and spinal canal measured from in vivo high-resolution anatomical magnetic resonance imaging," *Spine*, vol. 39, no. 4, pp. E262–E269, 2014.

[18] N. Khadka, X. Liu, H. Zander, J. Swami, E. Rogers, S. F. Lempka, and M. Bikson, "Realistic anatomically detailed open-source spinal cord stimulation (rado-scs) model," *bioRxiv*, p. 857946, 2019.

[19] S. Viljoen, B. D. Dalm, C. G. Reddy, S. Wilson, C. Smittkamp, G. T. Gillies, and M. A. Howard III, "Optimization of intradural spinal cord stimulator designs via analysis of thoracic spine imaging data," *Journal of Medical and Biological Engineering*, vol. 33, no. 2, pp. 193–198, 2013.

[20] S. F. Lempka, H. J. Zander, C. J. Anaya, A. Wyant, J. G. Ozinga IV, and A. G. Machado, "Patient-specific analysis of neural activation during spinal cord stimulation for pain," *Neuromodulation: Technology at the Neural Interface*, 2019.

[21] R. M. Levy, "Anatomic considerations for spinal cord stimulation," *Neuromodulation: Technology at the Neural Interface*, vol. 17, pp. 2–11, 2014.

[22] J. Holsheimer, "Which neuronal elements are activated directly by spinal cord stimulation," *Neuromodulation: Technology at the Neural Interface*, vol. 5, no. 1, pp. 25–31, 2002.

[23] J. Ladenbauer, K. Minassian, U. S. Hofstoetter, M. R. Dimitrijevic, and F. Rattay, "Stimulation of the human lumbar spinal cord with implanted and surface electrodes: a computer simulation study," *IEEE Transactions on Neural Systems and Rehabilitation Engineering*, vol. 18, no. 6, pp. 637–645, 2010.

[24] J. E. Arle, K. W. Carlson, L. Mei, and J. L. Shils, "Modeling effects of scar on patterns of

dorsal column stimulation," *Neuromodulation: Technology at the Neural Interface*, vol. 17, no. 4, pp. 320–333, 2014.

[25] H. McCann, G. Pisano, and L. Beltrachini, "Variation in reported human head tissue electrical conductivity values," *Brain topography*, pp. 1–34, 2019.

[26] Collaboration for NDT Education, "Conductivity and Resistivity Values for Nickel & Alloys," 2002. Available on: `https://www.nde-ed.org/GeneralResources/MaterialProperties/ET/Conductivity{_}Misc.pdf`.

[27] C. C. McIntyre, S. Mori, D. L. Sherman, N. V. Thakor, and J. L. Vitek, "Electric field and stimulating influence generated by deep brain stimulation of the subthalamic nucleus," *Clinical neurophysiology*, vol. 115, no. 3, pp. 589–595, 2004.

[28] B. De Leener, J. Cohen-Adad, and S. Kadoury, "Automatic segmentation of the spinal cord and spinal canal coupled with vertebral labeling," *IEEE transactions on medical imaging*, vol. 34, no. 8, pp. 1705–1718, 2015.

[29] M. Reina, A. Lopez-Garcia, M. Dittmann, and J. De Andrés, "Structural analysis of the thickness of human dura mater with scanning electron microscopy," *Revista espanola de anestesiologia y reanimacion*, vol. 43, no. 4, pp. 135–137, 1996.

[30] M. Reina, C. Franco, A. López, J. Dé Andrés, and A. Van Zundert, "Clinical implications of epidural fat in the spinal canal. a scanning electron microscopic study," *Acta anaesthesiologica belgica*, vol. 60, no. 1, p. 7, 2009.

[31] H. Zander, R. Graham, C. J. Anaya, and S. Lempka, "Anatomical and technical factors affecting the neural response to epidural spinal cord stimulation," *Journal of Neural Engineering*, 2020.

[32] W. Wesselink, J. Holsheimer, and H. Boom, "A model of the electrical behaviour of myelinated sensory nerve fibres based on human data," *Medical & biological engineering & computing*, vol. 37, no. 2, pp. 228–235, 1999.

[33] A. Richardson, C. McIntyre, and W. Grill, "Modelling the effects of electric fields on nerve fibres: influence of the myelin sheath," *Medical and Biological Engineering and Computing*, vol. 38, no. 4, pp. 438–446, 2000.

[34] G. Schalow, G. Zäch, and R. Warzok, "Classification of human peripheral nerve fibre groups by conduction velocity and nerve fibre diameter is preserved following spinal cord lesion," *Journal of the autonomic nervous system*, vol. 52, no. 2-3, pp. 125–150, 1995.

[35] B. K. van Veen, R. L. Schellens, D. F. Stegeman, R. Schoonhoven, and A. A. Gabreëls-Festen, "Conduction velocity distributions compared to fiber size distributions in normal human sural nerve," *Muscle & Nerve: Official Journal of the American Association of Electrodiagnostic Medicine*, vol. 18, no. 10, pp. 1121–1127, 1995.

[36] J. B. Ranck Jr, "Which elements are excited in electrical stimulation of mammalian central nervous system: a review," *Brain research*, vol. 98, no. 3, pp. 417–440, 1975.

[37] W. Tackmann and H. Lehmann, "Refractory period in human sensory nerve fibres," *European neurology*, vol. 12, no. 5-6, pp. 277–292, 1974.

[38] H. Feirabend, H. Choufoer, S. Ploeger, J. Holsheimer, and J. Van Gool, "Morphometry of human superficial dorsal and dorsolateral column fibres: significance to spinal cord stimulation," *Brain*, vol. 125, no. 5, pp. 1137–1149, 2002.

[39] M. Makino, K. Mimatsu, H. Saito, N. Konishi, and Y. Hashizume, "Morphometric study of myelinated fibers in human cervical spinal cord white matter," *Spine*, vol. 21, no. 9, pp. 1010–1016, 1996.

[40] W. A. Wesselink, J. Holsheimer, B. Nuttin, H. B. Boom, G. W. King, J. M. Gybels, and P. de Sutter, "Estimation of fiber diameters in the spinal dorsal columns from clinical data," *IEEE transactions on biomedical engineering*, vol. 45, no. 11, pp. 1355–1362, 1998.

[41] S. F. Lempka, C. C. McIntyre, K. L. Kilgore, and A. G. Machado, "Computational analysis of kilohertz frequency spinal cord stimulation for chronic pain management," *Anesthesiology: The Journal of the American Society of Anesthesiologists*, vol. 122, no. 6, pp. 1362–1376, 2015.

[42] C. C. McIntyre, A. G. Richardson, and W. M. Grill, "Modeling the excitability of mammalian

nerve fibers: influence of afterpotentials on the recovery cycle," *Journal of neurophysiology*, vol. 87, no. 2, pp. 995–1006, 2002.

[43] D. R. McNeal, "Analysis of a model for excitation of myelinated nerve," *IEEE Transactions on Biomedical Engineering*, no. 4, pp. 329–337, 1976.

[44] F. Rattay, "Analysis of models for external stimulation of axons," *IEEE transactions on biomedical engineering*, no. 10, pp. 974–977, 1986.

[45] M. P. Jensen and R. M. Brownstone, "Mechanisms of spinal cord stimulation for the treatment of pain: Still in the dark after 50 years," *European Journal of Pain*, vol. 23, no. 4, pp. 652–659, 2019.

[46] J. P. Miller, S. Eldabe, E. Buchser, L. M. Johanek, Y. Guan, and B. Linderoth, "Parameters of spinal cord stimulation and their role in electrical charge delivery: a review," *Neuromodulation: Technology at the Neural Interface*, vol. 19, no. 4, pp. 373–384, 2016.

[47] C. A. Bossetti, M. J. Birdno, and W. M. Grill, "Analysis of the quasi-static approximation for calculating potentials generated by neural stimulation," *Journal of neural engineering*, vol. 5, no. 1, p. 44, 2007.

[48] G. Molnar and G. Barolat, "Principles of cord activation during spinal cord stimulation," *Neuromodulation: Technology at the Neural Interface*, vol. 17, pp. 12–21, 2014.

[49] J. L. Durá, C. Solanes, J. De Andrés, and J. Saiz, "Programming strategies in post-implant clinical sessions: Usefulness of computer model to predict the paresthesia area displacement in the transversal direction," in *Invited Faculty Abstracts from the International Neuromodulation Societys 14th World Congress*, (Sidney, Australia), p. e343, May 2019.

[50] A. Taghva, E. Karst, and P. Underwood, "Clinical paresthesia atlas illustrates likelihood of coverage based on spinal cord stimulator electrode location," *Neuromodulation: Technology at the Neural Interface*, vol. 20, no. 6, pp. 582–588, 2017.

[51] M. Russo and J.-P. Van Buyten, "10-khz high-frequency scs therapy: a clinical summary," *Pain Medicine*, vol. 16, no. 5, pp. 934–942, 2015.

[52] A. Al-Kaisy, S. Palmisani, T. E. Smith, R. Carganillo, R. Houghton, D. Pang, W. Burgoyne, K. Lam, and J. Lucas, "Long-term improvements in chronic axial low back pain patients without previous spinal surgery: a cohort analysis of 10-khz high-frequency spinal cord stimulation over 36 months," *Pain Medicine*, vol. 19, no. 6, pp. 1219–1226, 2018.

[53] G. Barolat, "Epidural spinal cord stimulation: anatomical and electrical properties of the intraspinal structures relevant to spinal cord stimulation and clinical correlations," *Neuromodulation: Technology at the Neural Interface*, vol. 1, no. 2, pp. 63–71, 1998.

[54] M. Capogrosso, N. Wenger, S. Raspopovic, P. Musienko, J. Beauparlant, L. B. Luciani, G. Courtine, and S. Micera, "A computational model for epidural electrical stimulation of spinal sensorimotor circuits," *Journal of Neuroscience*, vol. 33, no. 49, pp. 19326–19340, 2013.

[55] C. J. Anaya, H. J. Zander, R. D. Graham, V. Sankarasubramanian, and S. F. Lempka, "Evoked potentials recorded from the spinal cord during neurostimulation for pain: a computational modeling study," *Neuromodulation: Technology at the Neural Interface*, vol. 23, no. 1, pp. 64–73, 2020.

[56] J. J. Struijk, J. Holsheimer, B. K. van Veen, and H. B. Boom, "Epidural spinal cord stimulation: calculation of field potentials with special reference to dorsal column nerve fibers," *IEEE transactions on biomedical engineering*, vol. 38, no. 1, pp. 104–110, 1991.

[57] K. Chakravarthy, M. A. Fishman, X. Zuidema, C. W. Hunter, and R. Levy, "Mechanism of action in burst spinal cord stimulation: Review and recent advances," *Pain Medicine*, vol. 20, no. Supplement_1, pp. S13–S22, 2019.

[58] H. Smits, M. Van Kleef, and E. Joosten, "Spinal cord stimulation of dorsal columns in a rat model of neuropathic pain: evidence for a segmental spinal mechanism of pain relief," *Pain*, vol. 153, no. 1, pp. 177–183, 2012.

[59] J. J. Struijk, J. Holsheimer, and H. B. Boom, "Excitation of dorsal root fibers in spinal cord stimulation: a theoretical study," *IEEE transactions on biomedical engineering*, vol. 40, no. 7,

pp. 632–639, 1993.

Supplementary information

1. Dimensions of the generalized and patient-specific spinal cord models

The geometrical parameters of the spinal cord (see figure S1) used in both generalized and patient-specific spinal cord models are listed in Table S1:
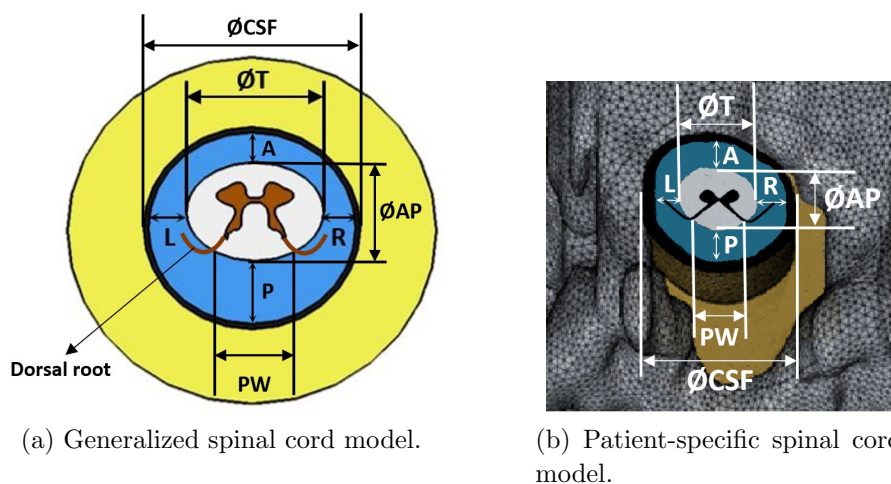

(a) Generalized spinal cord model.

(b) Patient-specific spinal cord model.

Figure S1: **Geometrical parameters of the spinal cord.** ØT: transversal diameter, ØAP: anteroposterior diameter, ØT: cerebrospinal fluid diameter, L: left, R: right, A: anterior; P: posterior and PW: posterior width.

Table S1: **Geometrical parameters of the generalized and patient-specific spinal cord model. The values used for the generalized models are extracted from Fradet et al. [17].**

| Parameter	General model (mm)	General model (mm)	General model (mm)	Patient-specific model (Patient 1) (mm)	Patient-specific model (Patient 2) (mm)
Vertebral level	T8	T9	T10	from T8 to T10	from T8 to T10
ØT	8.9	9	8.2	from 6.64 to 7.9	from 8.1 to 9.1
ØAP	6.2	6.5	6.6	from 5.36 to 6.2	from 5.3 to 6.55
PW	5.3	5.9	5.7	from 4.4 to 5.1	from 4.8 to 5.4
L	1.7	2.1	2.3	from 2.1 to 2.57	from 2 to 2.8
R	2	2.5	2.9	from 2.36 to 3.2	from 3 to 3.7
A	2	1.95	2.2	from 2.57 to 3.64	from 1.4 to 3
P	4.95	4.1	4	from 2.78 to 4.3	from 4.25 to 4.8
ØCSF	12.6	13.6	13.4	from 9 to 11.75	from 13.8 to 15.6
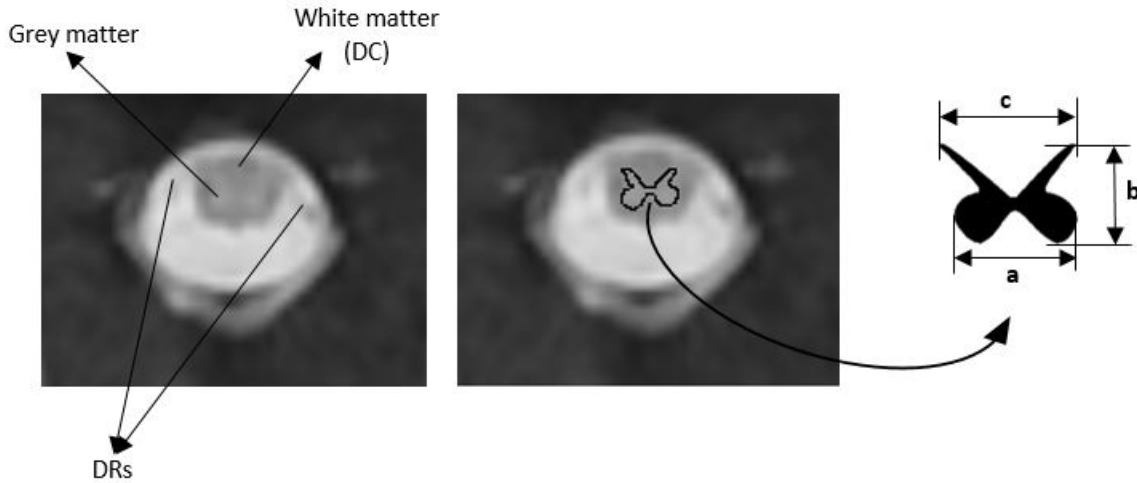
Figure S2: **Grey matter in the patient-specific model.** . Left: image capture of the patient's MRI where grey matter, white matter (where DC (dorsal columns) are located) and DRs (dorsal roots) can be differentiated. Right: manual representation of the gray matter shape in 2D. The dimensions obtained for grey matter are: a = 3.6 mm, b = 2 mm and c = 3.9 mm.

Grey matter tissue is not included in the volume conductor model of the patient-specific model when solving the FEM model to reduce the computational cost and because the electric field does not seem to be affected by grey matter [56]. A sensitivity analysis was performed to confirm that excluding grey matter does not affect the model predictions. As can be seen in Table S2, the results show small errors in the activation thresholds for the DC and DR nerve fibers (PT_{DC} and DT are 0.15% higher and PT_{DR} is 0.625% lower), in the recruitment ratio ($R_{DC/DR}$ is 0.294 % higher) and the activating area (AA is 1.85% higher), showing that grey matter can be ignored in this FEM design. However, grey matter shape is mimicked manually in 2D from the patient's MRI using COMSOL Multiphysics, as shown in figure S2 to calculate the posterior width (PW) and thus to obtain a realistic approximation to the DR location. We thus included the same grey matter shape in all axial views in the representation of the activation area in MATLAB R2017a but changed its location based on the previously measured PW value.

2. Equations of the myelinated nerve fiber model

The electrical diagram of the myelinated nerve fiber model is shown in figure S3(left). The membrane dynamics of the model includes sodium current, fast potassium current and leakage current. The gating parameters and membrane current equations are taken from Wesselink et al. [32]. The fiber geometry parameters and the internode parameters are taken from McIntyre et al. [42] and Richardson et al. [33]. The electrical parameters

of the nerve fiber model are shown in Table S3:

Applying Kirchhoff's law, the membrane currents in each compartment n is equal to the sum of the incoming axial currents and the sum of the capacitive and ionic currents (if the compartment is a Ranvier node) through the membrane. Two first-order differential equations are thus required: one for nodal compartments (see equation 1) and one for internodal compartments (see equation 2):

$$\frac{dV_n}{dt} = (G_a(V_{m,n-1} - 2V_{m,n} + V_{m,n+1} + V_{e,n-1} - 2V_{e,n} + V_{e,n+1}) - \pi dl I_{ion,n})/C_n, \qquad (1)$$

$$\begin{aligned}\frac{dV_n}{dt} = &(G_a(V_{m,n-1} - 2V_{m,n} + V_{m,n+1} + V_{e,n-1} - 2V_{e,n} + V_{e,n+1}) \\ &- G_m(V_{m,n} - V_{rest}))/C_m\end{aligned} \qquad (2)$$

Where G_a is the axial conductance between two compartments (mS), C_n is the nodal membrane capacitance (mF), G_m is the myelin membrane conductance (mS), C_m is the myelin membrane conductance (mF), $V_{(m,n)}$ is the membrane potential value at n compartment (mV), d is the nodal diameter (cm), l is the nodal length (cm), $I_{(ion,n)}$ is the sum of the ionic currents at n nodal compartment (mA/cm^2), V_{rest} is the resting potential (mV) and $V_{(e,n)}$ is the external electric potential in n compartment (mV).

The simulated action potential obtained from the new sensory nerve fiber model can be seen in figure S3(right). The action potential in a nerve fiber of 12.8 μm in diameter was stimulated by a rectangular monophasic stimulus of 300 μs pulse width and an amplitude of 1.2 times the threshold stimulus. The electrical behavior of the nerve fiber model fitted well to experimental data from human myelinated sensory nerve fibers.

Table S2: **Sensitivity analysis of excluding grey matter in the generalized volume conductor model. PT$_{DC}$: perception threshold in DC; PT$_{DR}$: perception threshold in DR; DT: discomfort threshold (1.4 PT$_{DC}$); R$_{DC/DR}$: recruitment ratio; AA: activating area; AD: activating depth. Stimulation parameters: guarded cathode (5(+),6(−),7(+)) and a rectangular monophasic pulse 300 μs duration.**

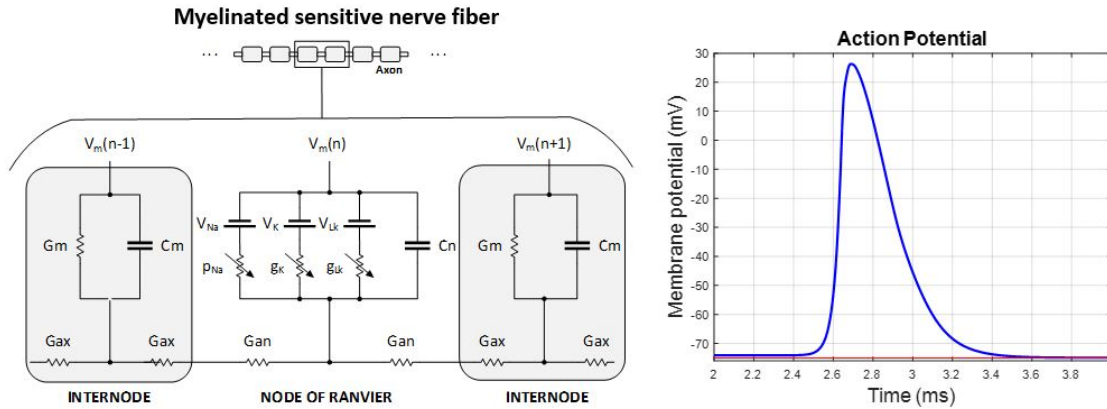| Source	PT$_{DC}$ (V)	PT$_{DR}$ (V)	DT (V)	R$_{DC/DR}$	AA (mm^2)	AD (μm)
FEM model with grey matter	3.8	11.2	5.32	0.34	1.62	500
FEM model without grey matter	3.806	11.13	5.328	0.341	1.65	500

Figure S3: **: Myelinated nerve fiber model diagram and electrical behavior.** Left: electrical diagram of the new sensitive nerve fiber model. Right: simulated AP at 37°C obtained from the new model (left). The horizontal line represents the rest potential considered (-75 mV). C_m: myelin capacitance; G_m myelin conductance; C_n: nodal capacitance; G_{ax}: axonal conductance in the internode; G_{an}: axonal conductance in the node; V_{Na}: sodium equilibrium potential; V_K: potassium equilibrium potential; V_{Lk}: leakage equilibrium potential; p_{Na}: sodium channel permeability; g_K: potassium channel conductivity; g_{Lk}: leakage channel conductivity; V_m: membrane potential.

3. Nerve fiber distribution

The procedure to include the nerve fiber distribution in the generalized and the patient-specific model is different.

As the geometry in the generalized model is symmetrical, 20 surfaces of 200×800 points of resolution are defined in COMSOL Multiphysics. Each surface is a point matrix which includes the position of the node of Ranvier in the model's x, y and z-axis and the electric potential value in that node after an electric field is applied. The first surface is located just in the DC border (see figure S4) and the following surfaces are located below each other at a separation of 50 μm. As each surface includes 100 longitudinally distributed fibers, we included a total of 2,000 fibers in the model, as shown in the axial view in figure S4. As the generalized model measures 88 mm, each nerve fiber has 66 nodes of Ranvier.

For the DR fibers two parametric surfaces of points (at left and right sides of the spinal cord) are defined in COMSOL Multiphysics that mimic the shape of a DR (see figure S4), i.e. they start in the CSF and enter the white matter in a curve (known as Dorsal Root Entry Zone (DREZ)) until reaching the dorsal horn of the grey matter. The distance between the left and right DREZ is PW, defined above in Section 1. Each surface includes 84 DR (1 mm spaced), so that a total of 168 DR fibers are included in the model. DR fibers have a diameter of 15 μm and consist of 5 nodes of Ranvier.

Since a low-thoracic segment was modeled, we chose to model the type A1 DR fiber as described by Struijk et al. [59].

As the geometry of the spinal cord is asymmetric in the patient-specific model, in order to locate the nerve fiber distribution, we first determined the middle line of the spinal cord (white matter) in COMSOL Multiphysics (see figure S5). The middle line is determined manually for each of the three vertebral levels (T8, T9 and T10). Using MATLAB R2017a, we then selected the points on the surface of the white matter closest to the points on the middle line that we had defined previously in COMSOL Multiphysics (see figure S5). The new middle line represents a nerve fiber located longitudinally along the white matter. From this nerve fiber we obtained the location of the rest of the nerve fibers. As in the generalized model, we included 100 nerve fibers per surface by selecting points 66-79 μm from the previous nerve fiber (50 nerve fibers from the middle nerve fiber to the left lateral and 50 nerve fibers from the middle nerve fiber to the right lateral). We then increased the depth to 50 μm to select the 100 nerve fibers on the next surface. A total of 20 rows of 100 nerve fibers were included in the model (2,000 nerve fibers), each with 64 nodes of Ranvier.

Table S3: **Electrical parameters of the nerve fiber model at body temperature (37°C).**

Symbol	Parameter	Value	Unit
p_{Na}	Na$^+$ channel permeability	$7.04 \cdot 10^3$	cm·s^{-1}
g_K	Slow K$^+$ channel conductivity	30	mS·cm^{-2}
g_{Lk}	Leak channel conductivity	60	mS·cm^{-2}
$[Na]_{out}$	Na$^+$ channels extracellular concentration	154	mM
$[Na]_{in}$	Na$^+$ channels intracellular concentration	30	mM
F	Faraday constant	96485	C/mol
R	Gas constant	8314.4	mV/K mol
T	Temperature	310.15	K
E_K	K$^+$ channel equilibrium potential	-75	mV
E_{Lk}	Leak channel equilibrium potential	-75.14	mV
V_{rest}	Resting potential	-75	mV
ρ_{ax}	Axoplasmic resistivity	70	Ωcm
c_n	Specific nodal capacitance	2.8	μF·cm^{-2}
c_m	Specific myelin capacitance	0.1	μF·cm^{-2}
g_m	Specific myelin conductance	1	mS·cm^{-2}
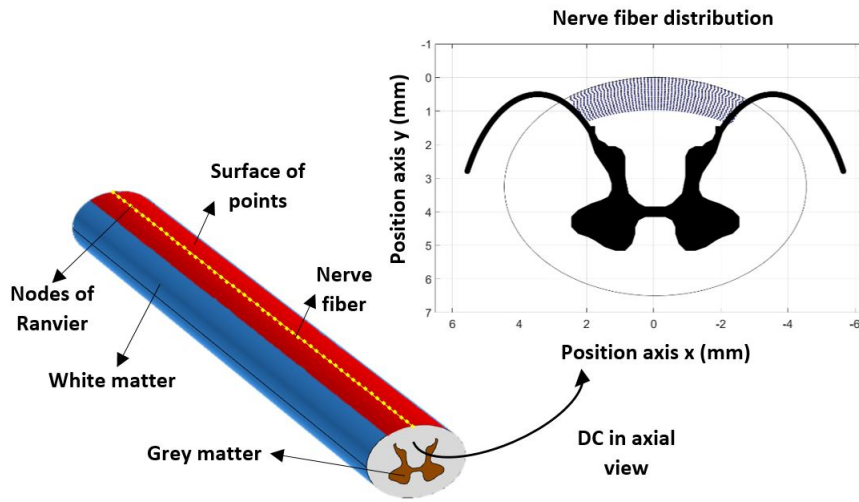
(a) Axial view of the nerve fiber distribution in the dorsal columns of the spinal cord (white matter).
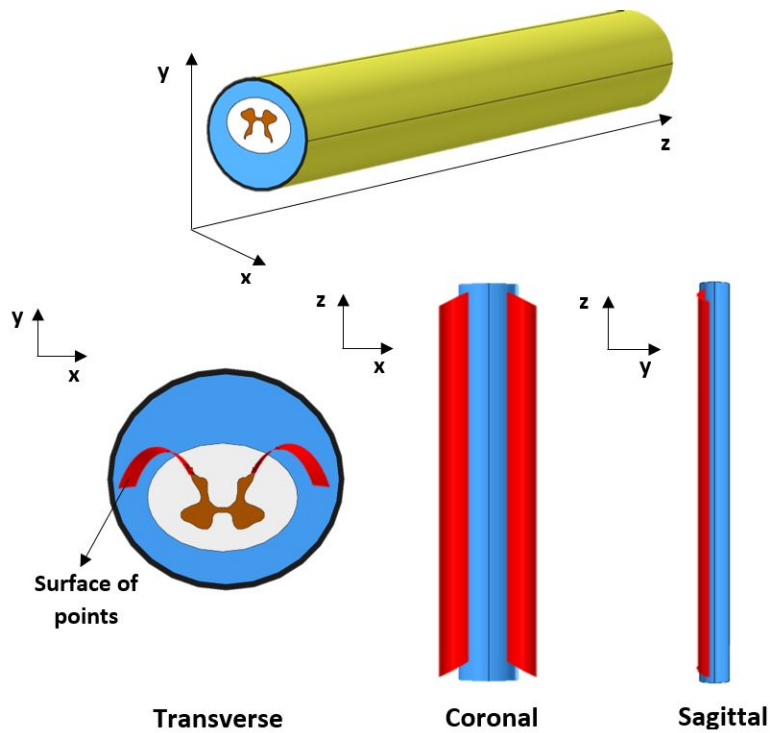
(b) DR nerve fibers distribution.

Figure S4: **Nerve fiber distribution in the generalized volume conductor model.** (a) Each blue point represents a nerve fiber in that position. (b) The figure above shows the definition of the x, y and z axes in the model. The figures below show the spatial location of the surfaces of points (shown in red) where the 168 DR fibers are included in transverse (left), coronal (center) and sagittal (right) views.

The same procedure as in the generalized model was followed for DR fibers. We defined two parametric surfaces of points (left and right sides of the spinal cord) but

(a) Middle line.
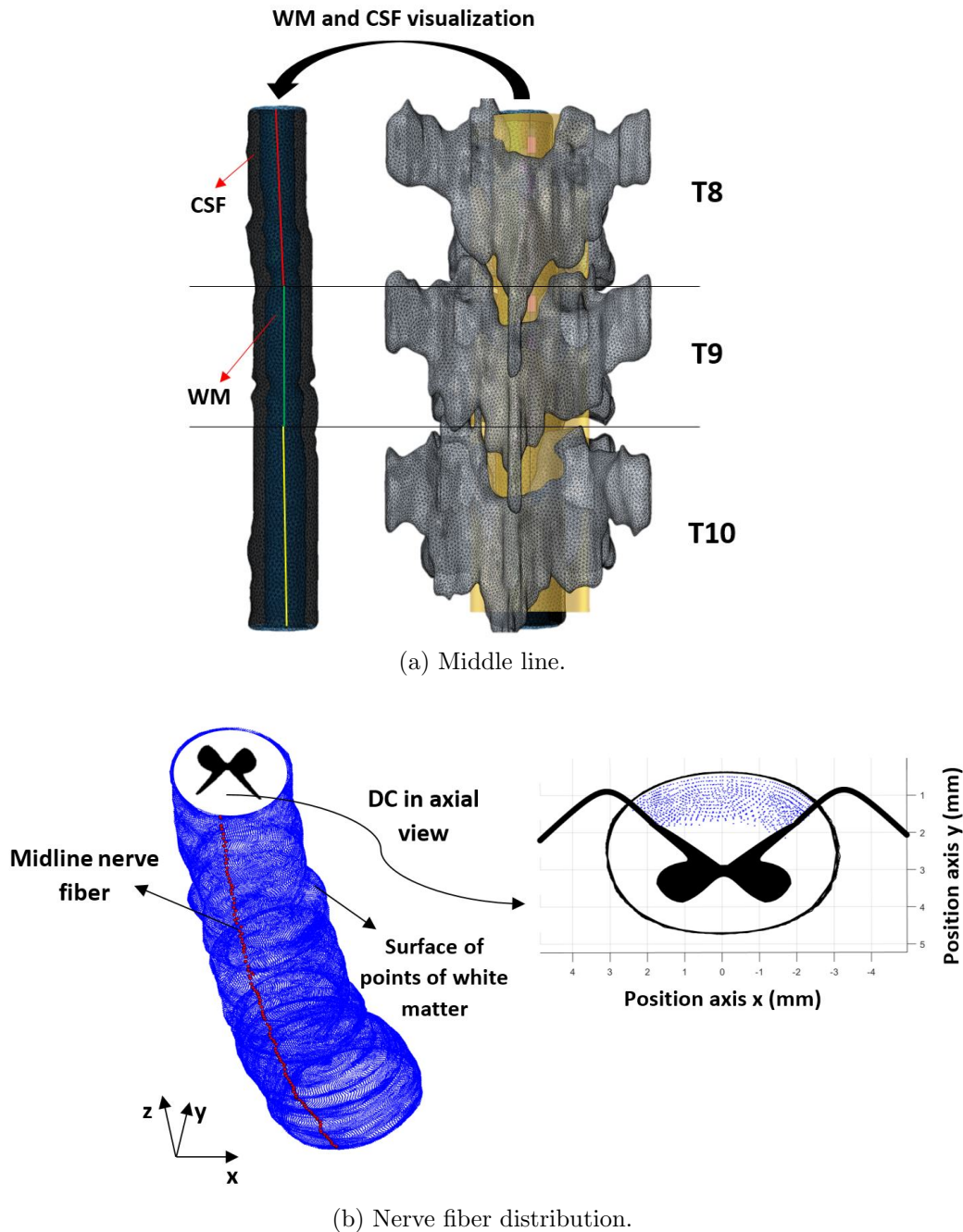

(b) Nerve fiber distribution.

Figure S5: **Definition of the middle line in DC of the patient-specific model.** (a) middle line is defined for the three vertebral level (T8 (red), T9 (green)and T10 (yellow)) manually in COMSOL Multiphysics. (b) after assigning the points (in positions x, y and z) on the surface of the white matter of the previously defined middle line the rest of the nerve fibers are selected applying a lateral separation of 66-79 μm (in x-axis) and a depth separation of 50 μm (in y-axis). Each blue point of the DC represents a node of Ranvier of a nerve fiber in that position.

in this case the curvature and spatial position are adapted manually at each vertebral
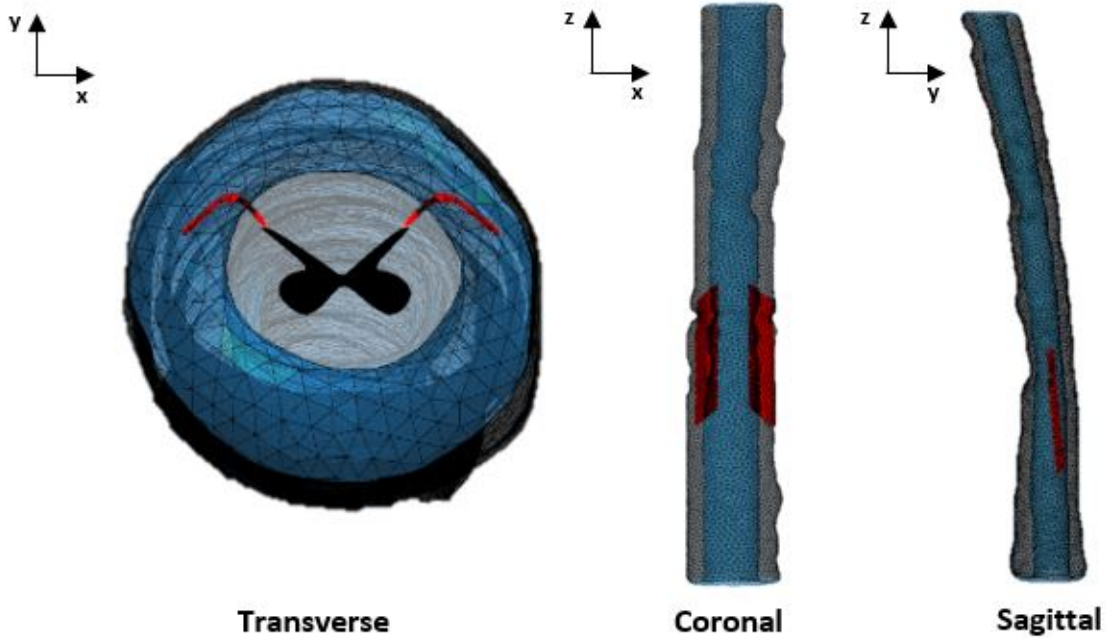
Figure S6: **DR nerve fibers distribution in the patient-specific model.** The surfaces of the (red) points defined to include the DRs in a specific zone of the spinal cord (between T9-T10) is shown for transverse (left), coronal (center) and sagittal (right) views. DR: dorsal root.

zone due to the geometric variation in the spinal cord and spinal canal of the model, as shown in figure S6. DR nerve fibers thus have between 5-7 nodes of Ranvier and a diameter of 15 μm.

For both the generalized and patient-specific models the points of the defined surfaces are exported from COMSOL Multiphysics to MATLAB R2017a. We then solve the model equations of the nerve fibers using backward Euler implicit integration with a time step of 0.001 ms to obtain the first activated nerve fiber on the DC surface. If an action potential is obtained PT is achieved. If not, we apply the minimum square method with a relative error of 0.05 V until PT is achieved. Threshold stimulation of DR nerve fibers is also calculated. A stimulation pulse is applied that consists of a rectangular-wave voltage pulse with 300 μs duration (a typical tonic stimulation waveform).

4. Volume conductor models implementation

In Table S4 the details for the boundary conditions and mesh resolution data of both generalized and patient-specific volume conductor models are shown.

Table S4: **Boundary conditions and mesh resolution data.**

Generalized volume conductor model

Boundary conditions	
External bounds	Zero current (*Electric insulation*)
Bounds of lead contacts	User-defined tension (*Electric potential*)
Mesh resolution	
Type	Adaptive
Number of elements	3,724,378
Maximum element size (mm)	1.94
Minimum element size (mm)	0.05
Maximum element grow rate	1.35
Resolution of curvature	0.3
Resolution of narrow regions	0.85

Patient-specific volume conductor model

Boundary conditions	
External bounds	Zero current (*Electric insulation*)
Bounds of lead contacts	User-defined tension (*Electric potential*)
Mesh resolution	
Type	Adaptive
Number of elements	12,229,088
Maximum element size (mm)	2.4
Minimum element size (mm)	0.024
Maximum element grow rate	1.3
Resolution of curvature	0.2
Resolution of narrow regions	1